UC Santa Barbara

UC Santa Barbara Electronic Theses and Dissertations

Title

Periodic Optomechanical Structures for the Study of Decoherence

Permalink

https://escholarship.org/uc/item/1qq7p57h

Author

Luna Rios, Jose Fernando

Publication Date

2020

Peer reviewed|Thesis/dissertation

eScholarship.org Powered by the California Digital Library
University of California

University of California
Santa Barbara

Periodic Optomechanical Structures for the Study of Decoherence

A dissertation submitted in partial satisfaction
of the requirements for the degree

Doctor of Philosophy
in
Physics

by

José Fernando Luna Ríos

Committee in charge:

Professor Dirk Bouwmeester, Chair
Professor Andreas Ludwig
Professor Andrea Young

September 2020

The Dissertation of José Fernando Luna Ríos is approved.

Professor Andreas Ludwig

Professor Andrea Young

Professor Dirk Bouwmeester, Committee Chair

August 2020

Periodic Optomechanical Structures for the Study of Decoherence

Copyright © 2020

by

José Fernando Luna Ríos

I dedicate this dissertation to my parents, who from an early age taught me the value of education and always encouraged my curiosity.

Acknowledgements

This work could not have been completed without the valuable contributions from a large number of people.

First of all, I would like to thank my adviser Dirk Bouwmeester for all his interest in my academic growth throughout my PhD. I am particularly grateful that he shared with me his passion for this project while I was still a prospective student. It was thanks to his support that I was able to come to UCSB.

I am very grateful for Matt's mentorship in the lab and in the cleanroom, and the discussions I had with him helped shape the course of my PhD. I am glad that I had the chance to work with Vitaliy, as it was very stimulating to exchange ideas and to witness his dedication and attention to details. I could not have wished for a better co-adviser than Wolfgang, and the tremendous amount of guidance I received from him was crucial at many stages of my PhD. To Frank, Hedwig, Kier, and Sven, I extend my gratitude for sharing their experience and for their helpful insights. I truly enjoyed working alongside Gesa, and I thank her for being so welcoming when I first visited Leiden, and every visit thereafter.

I thank all the brilliant students I worked with: Sameer, Elger, Matteo, David, Lucía, Crystal, Joey, Ian and Kellan, for their enthusiasm and effort. In many occasions, it was I who learned from them.

I want to thank the UCSB cleanroom staff for their help and support, and in particular Brian Thibeault for his critical advice in the fabrication of thin membranes. I would also like to acknowledge the impeccable work of Harmen van der Meer in the fabrication of all the necessary mechanical components for our experiments, and I thank Emiel Wiegers for machining some excellent sample holders for cleanroom processes.

I truly appreciate the support I received from professor Ania Jayich. I would like to thank her and Jeff Cady for sharing their expertise with our group. I managed to learn a lot while working with them, and I am very excited about the future of our joint project.

To my group members and office mates: Joe, John and Eric, I really enjoyed our friendly discussions during a shared car ride or over a meal.

I send special thanks to Fernando and to Petra, with whom I shared a home over the past several months, for keeping me company and making this difficult time a lot more manageable. To all my close my friends, thank you for all your words of encouragement.

I thank my sister Marisa for her fantastic work with two figures of this dissertation, and I am grateful to my brother Arturo, my parents Angelica and Nieves, who have always supported me in my endeavors.

Finally, I would like to thank and acknowledge the UC MEXUS-CONACYT collaboration for the support I received through a Doctoral Fellowship, which made my studies at UCSB possible.

Curriculum Vitæ

José Fernando Luna Ríos

Education

2017	M.A. in Physics, University of California, Santa Barbara
2014	B.Sc. in Physics, University of British Columbia

Publications

Newsom D.C., Luna F., Fedoseev V., Löffler W., Bouwmeester D. Optimal optomechanical coupling strength in multimembrane systems. Phys Rev A. 2020 Mar 20; 101(3): 033829.

Fedoseev V, Luna F., Löffler W., Bouwmeester D. Stimulated Raman adiabatic passage in optomechanics. arXiv:191111464 [physics, physics:quant-ph]. 2019 Nov 26

Weaver M.J., Newsom D., Luna F., Löffler W., Bouwmeester D. Phonon interferometry for measuring quantum decoherence. Phys Rev A. 2018 Jun 14; 97(6): 063832.

Sonar S, Fedoseev V., Weaver M.J., Luna F., Vlieg E., van der Meer H., et al. Strong thermomechanical squeezing in a far-detuned membrane-in-the-middle system. Physical Review A. 2018 Jul 3; 98(1).

Weaver M.J., Buters F., Luna F., Eerkens H., Heeck K., Man S., et al. Coherent optomechanical state transfer between disparate mechanical resonators. Nature Communications. 2017 Oct 10; 8(1): 824.

Buters F.M., Luna F., Weaver M.J., Eerkens H.J., Heeck K., de Man S., et al. Straightforward method to measure optomechanically induced transparency. Optics Express. 2017 May 29; 25(11): 12935.

Buters F.M., Heeck K., Eerkens H.J., Weaver M.J., Luna F., de Man S., et al. High-Q nested resonator in an actively stabilized optomechanical cavity. Applied Physics Letters. 2017 Mar 6; 110(10): 104104.

Weaver M.J., Pepper B., Luna F., Buters F.M., Eerkens H.J., Welker G., et al. Nested trampoline resonators for optomechanics. Applied Physics Letters. 2016 Jan 18; 108(3): 033501.

Abstract

Periodic Optomechanical Structures for the Study of Decoherence

by

José Fernando Luna Ríos

There are several unknown aspects about the decoherence mechanisms that cause the transition of a system from the quantum to the classical regime. In this work we present optomechanical systems, in which light couples to mechanical motion, as a suitable platform for the study of decoherence in macroscopic systems.

We start by discussing some of the features of optomechanical systems, focusing on the membrane-in-the-middle configuration. We then explain how optomechanical systems can be extended to include multiple modes, which enables different state transfer mechanisms, and we show an experimental demonstration of two such transfer schemes. We also explain how multimode systems can exhibit an enhanced optomechanical coupling rate for individual and collective mechanical modes.

Later we introduce periodic structures and how they can be applied at different scales in order to improve the performance of our optomechanical devices. We first analyze the vibrational modes of a thin membrane within the framework of linear elasticity and proceed to show how a phononic crystal reduces the dissipation of mechanical energy in the membrane. Next, we investigate an interference model for how a photonic crystal can enhance the reflectivity of a membrane for out-of-plane propagating radiation. We move on to outline the fabrication process for our optomechanical membrane devices.

We conclude with a theoretical proposal for a measurement of decoherence in a macroscopic superposition state. This proposal relies on the state transfer techniques discussed earlier and should be possible to implement with current technologies.

Contents

List of Figures

Chapter 1

Introduction

The subject of quantum mechanics is regarded by most as counterintuitive and arcane. Even today, almost 100 years after the formal emergence of the theory, many of its aspects remain a topic of active study. One of the questions that still lingers is the matter of why quantum phenomena are not observed in our daily lives. If the constituents of all matter behave according to the laws of quantum mechanics, why is it that we never find a pencil in a superposition state of being at two different places at once? Or why does a tennis ball never tunnel through the strings of a racket? It is this apparent absence of "quantumness" at the macroscopic scale that makes quantum mechanics seem so foreign.

The observation of quantum phenomena in systems of ever larger dimensions [1, 2] demonstrates that the laws of quantum mechanics are not limited to the atomic and molecular scales. Still, under standard temperature and pressure conditions, these systems do not display their quantum properties. Clearly, there is a transition between the "quantum" and the "classical" regime. When a system experiences said transition and its quantum properties are no longer observable, it is said to have undergone quantum decoherence.

1.1 Decoherence mechanisms

The most widely accepted mechanism behind quantum decoherence is known as environmentally induced decoherence [3, 4]. Stated simply, any real quantum system is never perfectly isolated and has some degree of coupling to its environment (which can be considered as another, much larger quantum system). Because of the coupling, the system and the environment will influence each other's evolution, and as time goes by, their respective states will become entangled, i.e., the state of the system will depend on the state of the environment, and vice versa. Unfortunately, in a real experiment it is unfeasible to completely keep track of the state of the environment. Thus, when we make a measurement on our system, we are only obtaining a partial picture of a larger whole (our quantum system of interest plus the environment). Then, the outcome of our incomplete measurement will reveal the state of the system, averaged over all the possible states of the environment (which we cannot measure). It is this "averaging" of the state that results in its apparent loss of quantum coherence. Formally speaking, when we perform a measurement only on the quantum system of interest, we are probing a reduced density matrix that is the result of tracing out all of the environment's degrees of freedom. Then, the argument is that systems of larger dimension or with a higher number of components are more strongly coupled to the environment, which in turn results in a faster entanglement and consequently, decoherence. Therefore, for an ordinary macroscopic object which is very strongly coupled to its surroundings (through air molecules bouncing off of it, light being reflected or absorbed, etc.) the rate at which decoherence happens is so fast that we could never expect to observe any quantum behaviour.

Other mechanisms for quantum decoherence have been proposed. The model of gravitationally induced decoherence [5], for example, is a consequence of applying the principles of quantum mechanics and general relativity to a system in a superposition state where its mass exists in distinct spatial distributions. For such a system, there is a superposition of two different space-times within which time evolution is ill-defined. This leads to an uncertainty in the energy of the system ΔE which results in the superposition state being unstable and having a lifetime on the order of $\hbar/\Delta E$, as dictated by the uncertainty principle.

A different decoherence mechanism is proposed by the model of continuous spontaneous localization [6]. The idea behind this model is that the time evolution of every quantum state is constantly subject to a stochastic collapse process that localizes the corresponding wave function within a certain range. This occurs without the need of any interaction with an external system (such as a measurement device or an observer).

The two models above have in common that the strength of the proposed decoherence mechanism depends on the scale of the system. Thus, systems at the atomic scale are mostly unaffected by such mechanisms, while larger systems experience a very fast decay of their quantum coherence, providing a possible explanation for why quantum mechanics seems to break down as objects get larger and more complex.

1.2 Optomechanics for the study of decoherence

The long-term goal of our research is to quantitatively measure the decoherence rate of a macroscopic superposition state, in a system whose size and complexity place it at a scale where we could detect effects from the decoherence mechanisms mentioned above. By doing so, we intend to gain a better understanding of the actual process (or processes) that prevents quantum behaviour from being exhibited at large scales.

A suitable platform to perform such an experiment is optomechanics. Optomechanical systems combine the use of light for the preparation, manipulation and readout of quantum states, with the versatility and robustness of mechanical resonators. Further-

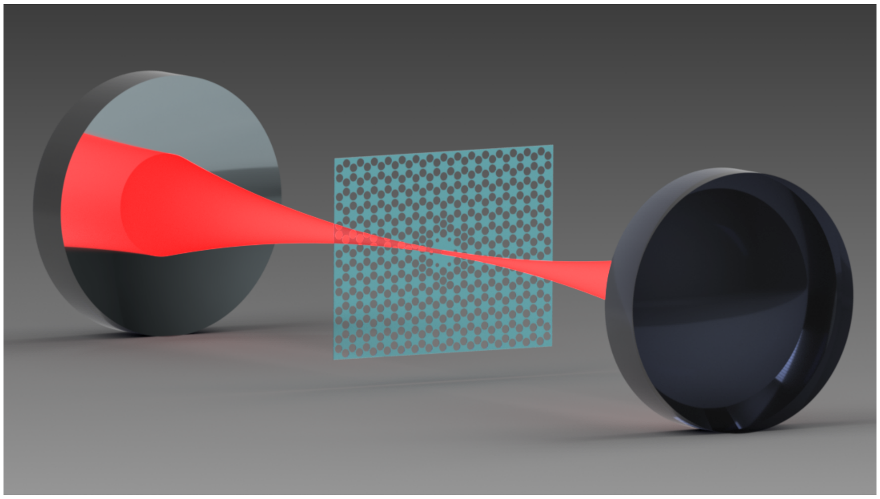

Figure 1.1: Our optomechanical system, consisting of a thin vibrating membrane inside an optical cavity.

more, optomechanical systems can be constructed at many different scales, granting the ability to operate at different regimes. In chapter 2 we briefly introduce some of these systems and then present the optomechanical interaction and the physical phenomena that arise from it, with an emphasis on how they can be exploited to control the state of a mechanical resonator. In the same chapter, we describe our implementation of an optomechanical system, depicted in Fig. 1.1, which is that of a thin vibrating membrane inside an optical cavity. Chapter 3 extends the optomechanical interaction to multimode systems, with a focus on state transfer interactions.

A substantial portion of our research has been devoted to improving the parameters of our experimental setup in order to increase the feasibility of our intended experiments. In this regard, significant progress has been made through the use periodic structures that modify the propagation of acoustic and electromagnetic waves. Chapter 4 gives a brief summary of the properties of periodic structures, as an introduction for the two subsequent chapters. In chapter 5 we discuss the mechanical membranes that we use in our experiments, and how we employ phononic crystals to improve their mechanical quality. Chapter 6 describes the application of photonic crystals for the enhancement of the optomechanical coupling strength of our system. We have included an appendix that discusses the numerical tools that we employ in the design of the periodic structures. Then, in chapter 7, we present a general description of the fabrication process of our optomechanical devices.

In chapter 8, we explain how our optomechanical system should allow us to prepare a superposition state and perform decoherence measurements over millisecond timescales, long enough for the mentioned decoherence mechanisms to manifest. We finish this work in chapter 9 with a short conclusion and an outlook of where our research is headed.

Chapter 2

Cavity Optomechanics

Optomechanics is the study of the interaction between electromagnetic radiation and mechanical motion [7]. This interaction occurs because light carries momentum and can therefore impart a force onto an object. This force, known as **radiation pressure force**, is normally too weak for us to perceive. However, the dynamics of an object with a small mass can be greatly influenced by radiation pressure. A commonly cited example of the optomechanical interaction in nature is that of the tails of a comet pointing away from the sun, due to radiation pressure from sunlight.

As a matter of fact, an object does not need to be very small or very light in order to be significantly affected by radiation pressure. This is because the optomechanical interaction can be enhanced by placing the object inside an optical resonator, such as a cavity formed by two mirrors. As a result, optomechanical effects have been studied and applied in systems spanning a range of mass and frequency that extends by several orders of magnitude. For example, optomechanical systems can be as small as a cloud of atoms with a mass of about 10 attograms[1] and a collective motional frequency of hundreds of kHz [8], or as large as a suspended mirror weighing 250 grams and oscillating at 1 Hz [9].

---

[1] 1 attogram = 10^{-18} gram

Each of these drastically distinct systems has a use for different experiments, including gravitational wave detection [10], magnetic sensing [11], fundamental tests of quantum mechanics [12], and measurement of quantum decoherence [13], to name a few.

In this chapter, we give an introduction to cavity optomechanics following the work in [7]. We begin by describing separately the mechanical and optical components of an optomechanical system. Next, we introduce the optomechanical interaction for systems in two different configurations. We continue by discussing the Hamiltonian that describes the optomechanical interaction and the phenomena that arise from it. The last section of the chapter presents the dominant loss channels that affect optomechanical systems.

2.1 Optical cavities

An optical cavity is a resonator for electromagnetic waves that supports optical modes with frequencies given by a resonance condition. In the case of a cavity of length L formed by two mirrors, the resonance condition is met by all modes with frequencies

$$\omega_n = \frac{n\pi c}{L} \tag{2.1}$$

for some positive integer n, with c being the speed of light. From this condition, we can see that the modes are evenly spaced in frequency by the **free spectral range** of the cavity $\omega_{FSR} = \pi c/L$. We will now focus on one of these resonant modes and we will label its frequency as ω_c.

Light that is not resonant with the cavity is mostly reflected on incidence. Conversely, the cavity becomes transmissive for incident light that is close to resonance. This behaviour is quantified by the **cavity linewidth** κ, which determines the width of the transmission peaks in frequency space (see Fig. 2.1). The linewidth also provides a

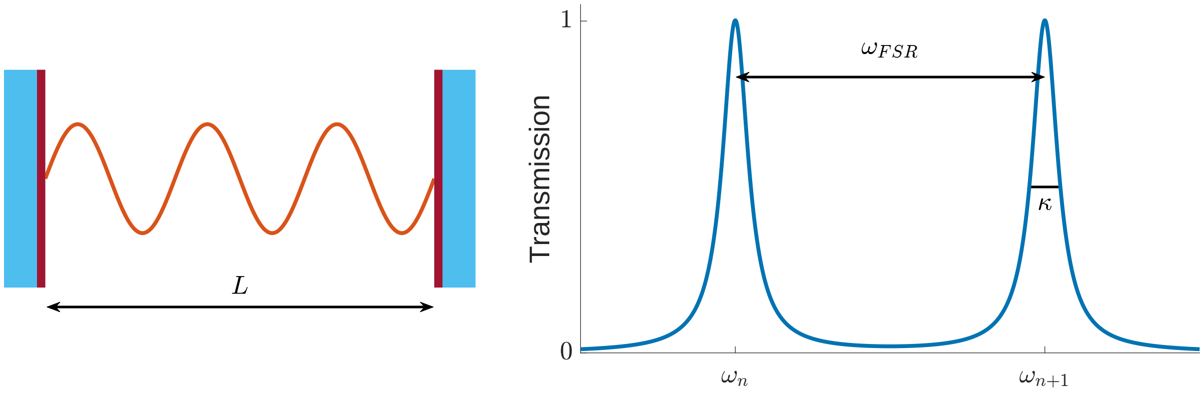

Figure 2.1: (left) An optical cavity formed by two mirrors spaced by a distance L. (right) Transmission spectrum of an optical cavity. The free spectral range ω_{FSR} and cavity linewidth κ are shown.

measure of how quickly light stored inside the cavity leaks out. In other words, κ is the decay rate of the electromagnetic energy inside the cavity. An optical cavity is commonly characterized by its **finesse**, given by $\mathcal{F} = \omega_{FSR}/\kappa$. A larger finesse implies narrower resonances and longer storage times for light inside the cavity.

Since the amplitude of electromagnetic waves oscillates harmonically in time, they can be described by the standard harmonic oscillator Hamiltonian. Then, in a quantum mechanical representation, the Hamiltonian of the cavity mode is

$$H = \hbar\omega_c \hat{a}^\dagger \hat{a} + \frac{\hbar\omega_c}{2}, \tag{2.2}$$

where $\hbar$ is the reduced Planck constant, $\hat{a}$ is the amplitude of the optical mode, and $\hat{a}^\dagger\hat{a} = n_c$ is the number of photons inside the cavity. Here we have excluded any driving or dissipation terms. In subsequent discussions, we will also ignore the term describing the zero-point energy of the mode, since it does not affect the dynamics.

In subsequent sections, it will be useful to know the average number of photons that are circulating inside the cavity when we drive it with a laser. Employing the input-output formalism [14], we can calculate the average number of intracavity photons for a cavity drive of frequency ω_L and power P

$$\bar{n}_c = \frac{P}{\hbar\omega_L}\frac{\kappa_{ex}}{(\kappa/2)^2 + \Delta^2}, \tag{2.3}$$

where the ratio κ_{ex}/κ is the input coupling, and $\Delta = \omega_L - \omega_c$ is the detuning of the laser drive.

2.2 Mechanical resonators

The mechanical element in an optomechanical system can take on many different shapes and sizes. Whatever the structure, its motional degrees of freedom can be decomposed into normal modes. We will pick one such mode, and denote by $x(t)$ the amplitude of its motion as a function of time. Under a linear elastic treatment, which we discuss more fully in chapter 5, $x(t)$ obeys the equation of motion for a harmonic oscillator. A mechanical mode with resonant frequency Ω_m can then be described quantum mechanically as before with the standard harmonic oscillator Hamiltonian

$$H = \hbar\Omega_m \hat{b}^\dagger \hat{b}. \tag{2.4}$$

Notice that we have omitted the zero-point energy term as discussed in the previous section. Here $\hat{b}^\dagger\hat{b}$ is the number of phonons in the mechanical mode. The operator $\hat{b}$ is related to the amplitude of the motion by

$$\hat{x} = x_{ZPF}(\hat{b} + \hat{b}^\dagger), \tag{2.5}$$

where $x_{ZPF} = \sqrt{\frac{\hbar}{2m_{eff}\Omega_m}}$ are the zero-point fluctuations of the mechanical mode, and the mode's effective mass m_{eff} is determined by relating the average of the potential

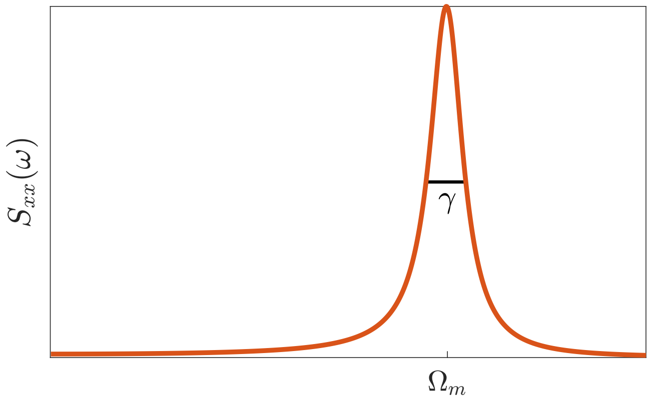

Figure 2.2: Noise power spectral density of a mechanical resonator. The peak is centered at the mechanical resonance frequency Ω_m and has a linewidth equal to the mechanical damping rate γ.

energy to the mean square amplitude of motion

$$\langle U_{pot}\rangle = \frac{m_{eff}\Omega_m^2 \langle x^2(t)\rangle}{2}. \tag{2.6}$$

Any real mechanical mode will have a finite amount of damping, characterized by the **mechanical damping rate** γ at which mechanical energy gets dissipated. When measuring the motion of a mechanical resonator, it is common to obtain its **noise power spectral density** $S(\omega)_{xx}$ in frequency space, which we define as the Fourier transform of the autocorrelation function of $x(t)$

$$S(\omega)_{xx} = \int_{-\infty}^{\infty} \langle x(t)x(0)\rangle e^{i\omega t}dt. \tag{2.7}$$

The noise power spectral density of a mechanical resonator will exhibit a peak at Ω_m with a linewidth γ, as shown in Fig. 2.2. The **mechanical quality factor** $Q = \Omega_m/\gamma$ is commonly used to characterize the performance of a mechanical resonator, and it gives the number of coherent oscillations a mode will perform before its mechanical energy decreases by a factor of e. A higher Q means the resonator will oscillate coherently for a

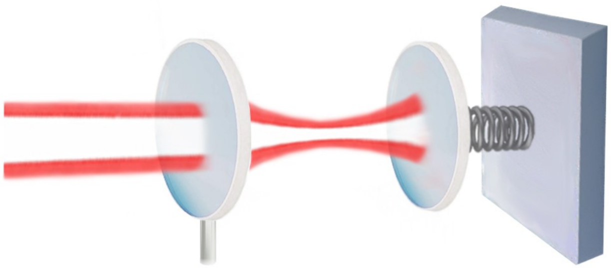

Figure 2.3: An optomechanical cavity. One of the end mirrors is free to oscillate, and is affected by the radiation pressure force from the optical field inside the cavity.

longer time.

2.3 Optomechanical interaction

As we mentioned at the beginning of the chapter, the optomechanical interaction is caused by the radiation pressure force that light exerts on a mechanical object. To illustrate the interaction, we resort to the prototypical example of an optical cavity with an oscillating end mirror, schematically depicted in Fig. 2.3. In essence, this system is composed of two coupled harmonic resonators, one optical, the other mechanical. The coupling is manifested in the interdependence between the intensity of the intracavity field and the position of the movable mirror. As the mirror moves, the length of the cavity, and therefore its resonance frequency, changes. This in turn modifies the amount of light that builds up inside the cavity and consequently the amount of radiation pressure force that affects the motion of the mirror. From a Hamiltonian perspective, we can describe this system by simply adding the Hamiltonians of the individual resonators to obtain

$$H = \hbar\omega_c(x)\hat{a}^\dagger\hat{a} + \hbar\Omega_m\hat{b}^\dagger\hat{b}. \tag{2.8}$$

Here, x refers to the displacement of the moving mirror from some equilibrium cavity length L. Notice that we have made explicit the dependence of the cavity's resonance frequency on the position of the mirror. From Eq. 2.1, we have to first order in x

$$\omega_c(x) = \frac{n\pi c}{L + x} \approx \omega_c(0) - Gx, \tag{2.9}$$

$$G = -\left.\frac{d\omega_c(x)}{dx}\right|_{x=0} = \omega_c(0)/L. \tag{2.10}$$

Then, setting $\omega_c(0) = \omega_c$, the Hamiltonian of the system becomes

$$H = \hbar\omega_c \hat{a}^\dagger \hat{a} + \hbar\Omega_m \hat{b}^\dagger \hat{b} - \hbar G \hat{x} \hat{a}^\dagger \hat{a}. \tag{2.11}$$

It is the third term of this expression that gives rise to the optomechanical interaction. Using Eqn. 2.5, we can rewrite the interaction term as

$$H_{int} = -\hbar g_0 (\hat{b} + \hat{b}^\dagger) \hat{a}^\dagger \hat{a}, \tag{2.12}$$

where $g_0 = Gx_{ZPF}$ is the **single-photon optomechanical coupling rate**. As the name implies, g_0 gives a measure of the mirror displacement generated by a single photon inside the cavity. At the beginning of the chapter we mentioned that the optical cavity enhances optomechanical effects. This is because the presence of the cavity allows photons to interact with the mechanical oscillator multiple times before they leak out. The **multi-photon optomechanial coupling rate** $g = \sqrt{\bar{n}_c} g_0$ quantifies this enhancement, with $\bar{n}_c$ being the average number of intracavity photons defined in section 2.1. This parameter determines the speed at which optomechanical interactions occur and is therefore critical for the successful implementation of our decoherence experiments, which we discuss in chapter 8.

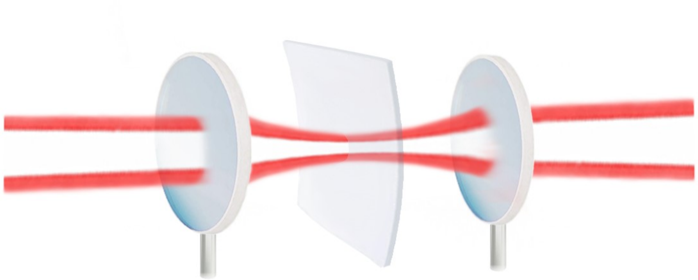

Figure 2.4: A membrane-in-the-middle optomechanical system. The motion of the membrane and the optical field inside the cavity are coupled through radiation pressure.

Another important figure of merit is the **cooperativity**, $C = 4g_0^2\bar{n}_c/\kappa\gamma$. This quantity determines the strength of **optomechanically induced transparency**, where the transmission through the optomechanical cavity is greatly modified in the presence of a control beam [15, 16]. This phenomenon is usually employed to accurately measure the optomechanical coupling rate. Furthermore, the cooperativity determines the effectiveness of optomechanical cooling, which we discuss in section 2.4.1. Although in principle one could increase the power of the cavity drive to increase g and C, in practice, aspects such as optical absorption or measurement back-action limit the amount of laser power that can be used. Therefore, it is better to start with a large g_0 to avoid the need for large drive powers.

2.3.1 Membrane-in-the-middle systems

An alternative implementation for an optomechanical system is that of a fixed optical cavity with a vibrating membrane at its center, as shown in Fig. 2.4. This membrane-in-the-middle configuration, originally introduced in [17], decouples the mechanical and optical properties of the system. This allows us to optimize the design of the mechanical

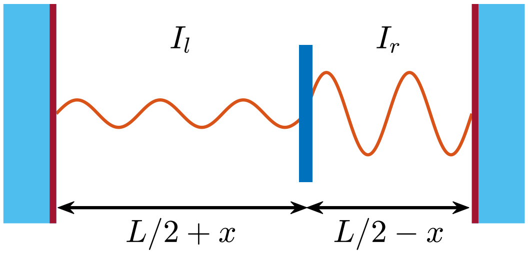

Figure 2.5: Two coupled subcavities in a membrane-in-the-middle system. The portion of the total optical field contained in each subcavity is determined by the position of the membrane at a wavelength scale.

and optical resonators independently, so that improvements in one do not come at the expense of loss in performance in the other. This setup configuration is also suitable for use with multiple membranes. In section 3.3 we will see that such a system can be used for the study of collective mechanical modes.

The optical field and the motion of the membrane are coupled by radiation pressure, and the system is described by the same optomechanical Hamiltonian presented in the previous section. However, the details of the coupling are slightly different. As before, L and ω_c are the length and resonance frequency of the optical cavity, and x is now the position of the membrane with respect to the cavity center. Furthermore, let r and θ_r denote the magnitude and phase of the membrane's field reflection coefficient. The presence of the membrane effectively splits the cavity into two coupled subcavities, as shown in Fig. 2.5. An important feature is that the intensity of the cavity field is not necessarily the same on both sides of the membrane, which causes a radiation pressure differential across it [18]. The single-photon optomechanical coupling rate is proportional to this differential

$$g_0 = x_{ZPF}\frac{\omega_c}{L}A(I_r - I_l). \tag{2.13}$$

Here, I_l (I_r) is the relative field intensity of the subcavity to the left (right) of the membrane, and A is the absolute intensity of the optical mode. These dimensionless intensities are normalized such that $I_r + I_l = 1$, and $A = [I_l(1/2 + x/L) + I_r(1/2 - x/L)]^{-1}$. The ratio of the field intensities is determined by the membrane's position, and is given by

$$\frac{I_r}{I_l} = \frac{1 - 2r\cos(2\phi + \theta_r) + r^2}{1 - r^2}, \tag{2.14}$$

where $\phi = 2\pi(L/2 + x)/\lambda$ is the phase of the field at the membrane, and $\lambda = 2\pi c/\omega_c$ is the wavelength of the light. Here, we have assumed that the thickness of the membrane is much smaller than λ. Notice that the intensity ratio varies on a wavelength scale. This means g_0 can be tuned, and even made to vanish, by making wavelength-scale adjustments to the position of the membrane. Another important aspect, not immediately apparent from expressions 2.13 and 2.14, is that to a very good approximation g_0 increases linearly with r. For this reason, we try to increase the reflectivity of the membranes by patterning them with photonic crystals, as discussed in chapter 6.

2.4 The optomechanical Hamiltonian

In the previous section, we saw that an optomechanical system has a Hamiltonian composed of three terms

$$H = \hbar\omega_c\hat{a}^\dagger\hat{a} + \hbar\Omega_m\hat{b}^\dagger\hat{b} - \hbar g_0(\hat{b} + \hat{b}^\dagger)\hat{a}^\dagger\hat{a}. \tag{2.15}$$

The first two describe independent harmonic oscillators and the third gives the interaction that arises from the dependence of the cavity resonance frequency on the position of the mechanical oscillator. Because the interaction term in Eqn. 2.15 involves the product of three operators, the equations of motion that result from it are nonlinear and cannot be analytically solved. Then, in order to understand the dynamics of the system, we work with a "linearized" version of the Hamiltonian [7].

Before proceeding, it will be useful to move into a frame rotating at the laser drive frequency by applying a unitary operator $\hat{U}(t) = \exp(i\omega_L \hat{a}^\dagger \hat{a} t)$, after which, the Hamiltonian becomes

$$H = -\hbar\Delta\hat{a}^\dagger\hat{a} + \hbar\Omega_m\hat{b}^\dagger\hat{b} - \hbar g_0(\hat{b} + \hat{b}^\dagger)\hat{a}^\dagger\hat{a}. \tag{2.16}$$

Recall that $\Delta = \omega_L - \omega_c$ is the laser detuning. The idea behind the linearization is to obtain the dynamics of the system around a steady state of the cavity. To implement this, we separate the optical mode amplitude into an average value $\alpha = \langle\hat{a}\rangle = \sqrt{\bar{n}_c}$ and a fluctuating part as follows: $\hat{a} \rightarrow \alpha + \hat{a}$, where $\hat{a}$ now denotes fluctuations around the average value α, which we set to be real without loss of generality. With this decomposition, we can expand the interaction term as

$$H_{int} = -\hbar g_0(\hat{b} + \hat{b}^\dagger)[\alpha^2 + \alpha(\hat{a} + \hat{a}^\dagger) + \hat{a}^\dagger\hat{a}]. \tag{2.17}$$

The first resulting term $-\hbar g_0(\hat{b} + \hat{b}^\dagger)\alpha^2$ describes a constant force that will displace the equilibrium position of the mechanical resonator by a fixed amount. We can ignore this term after appropriately redefining $\hat{x}$ to incorporate this shift. From the remaining terms, we only keep those linear in $\hat{a}$, since the quadratic term will be smaller by a factor $\hat{a}$. Then, the interaction term becomes

$$H_{int} = -\hbar g(\hat{a}^\dagger\hat{b} + \hat{a}\hat{b}^\dagger + \hat{a}^\dagger\hat{b}^\dagger + \hat{a}\hat{b}), \tag{2.18}$$

where we used $g = g_0\sqrt{\bar{n}_c}$. This linear approximation will be valid even if the optical field amplitude is small, provided that our system is not in the single-photon strong coupling regime ($g_0 \gg \kappa$), which is not usually achievable with the type of optomechanical systems that we employ. In the interaction picture, the operators $\hat{a}$ and $\hat{b}$ evolve according to the "bare" portion of the Hamiltonian in Eq. 2.16, and the terms of the linearized interaction

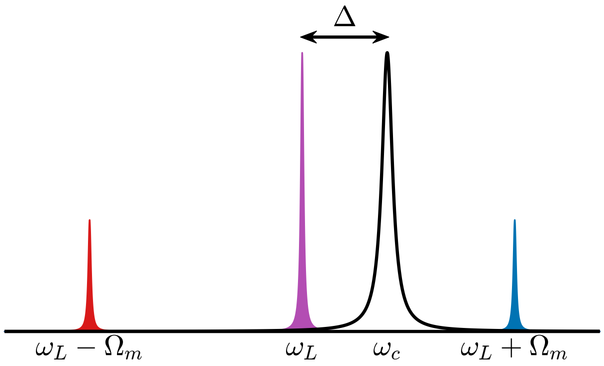

Figure 2.6: Sidebands generated on the optical field due to mechanical motion. The sidebands are separated in frequency by Ω_m from the carrier. Depending on the detuning Δ, either one of the sidebands can be enhanced by the cavity.

Hamiltonian in Eq. 2.18 acquire a time-varying phase:

$$H_{int} = -\hbar g(\hat{a}^\dagger \hat{b} e^{i(\Delta+\Omega_m)t} + \hat{a}\hat{b}^\dagger e^{-i(\Delta+\Omega_m)t} + \hat{a}^\dagger \hat{b}^\dagger e^{i(\Delta-\Omega_m)t} + \hat{a}\hat{b} e^{-i(\Delta-\Omega_m)t}). \tag{2.19}$$

If we make the rotating wave approximation (RWA), different terms will be dominant, depending on the detuning of the laser drive. This relative enhancement or suppression of terms can be understood from an alternative perspective. As shown in Fig. 2.6, the motion of the mechanical resonator modulates the amplitude of the field inside the cavity, generating a pair of sidebands separated in frequency by Ω_m from the carrier wave. Each of the sidebands is associated with two of the four interaction terms in Eqn. 2.19. The presence of the cavity can enhance one of these sidebands and make the corresponding terms in the Hamiltonian dominant. This effect will be more prominent for systems that are sideband-resolved ($\Omega_m \gg \kappa$).

2.4.1 Red-detuning

When the laser is red-detuned by one mechanical frequency, i.e., $\Delta = -\Omega_m$, the anti-Stokes sideband with frequency $\omega_L + \Omega_m$ is enhanced by the cavity (see Fig. 2.7), and

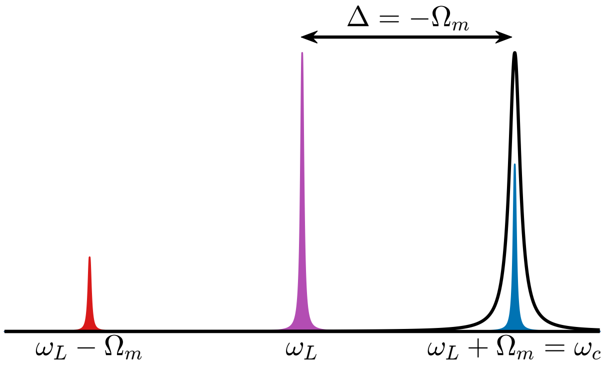

Figure 2.7: Sideband position relative to the cavity resonance when the laser drive is red-detuned ($\Delta = -\Omega_m$).

the dominant terms of the interaction Hamiltonian are

$$H_{int} = -\hbar g(\hat{a}^\dagger \hat{b} + \hat{a}\hat{b}^\dagger). \tag{2.20}$$

This "beamsplitter" interaction exchanges quanta between the optical and mechanical modes. The enhancement of the anti-Stokes sideband results in photons from the laser drive being preferentially upconverted to the cavity resonance by absorbing a phonon from the mechanical oscillator. When operating in the weak coupling regime ($g \ll \kappa$), the interaction leads to optomechanical cooling (also known as optomechanical damping). This is because once a photon is upconverted, it leaks out of the cavity faster than it can be downconverted back (which would generate a phonon in the mechanics). At optical frequencies, the cavity mode is effectively coupled to an environment with zero thermal occupation. Thus, the overall result of the interaction is the extraction of energy out of the mechanical resonator.

For the case of strong coupling ($g \gg \kappa$) the beamsplitter interaction hybridizes the optical and mechanical modes and the excitations become of mixed optical and mechanical nature. Our system does not operate in this regime.

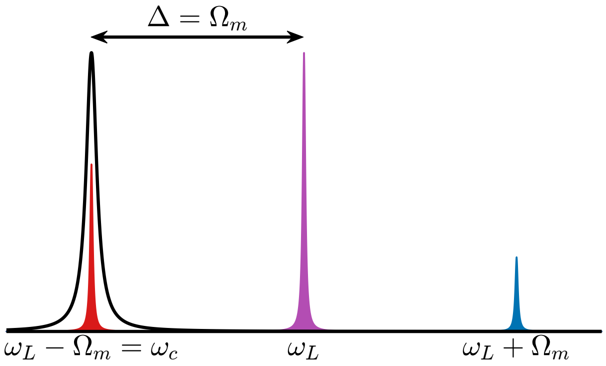

Figure 2.8: Sideband position relative to the cavity resonance when the laser drive is blue-detuned ($\Delta = \Omega_m$).

2.4.2 Blue-detuning

If we instead blue-detune the laser drive by one mechanical frequency, i.e., $\Delta = \Omega_m$, it is the Stokes sideband with frequency $\omega_L - \Omega_m$ that gets enhanced by the cavity (see Fig. 2.8), and the dominant terms of the interaction Hamiltonian are

$$H_{int} = -\hbar g(\hat{a}^\dagger \hat{b}^\dagger + \hat{a}\hat{b}). \tag{2.21}$$

This interaction, referred to as "two-mode squeezing", is often compared to parametric amplification, because a drive photon generates a pair of a downconverted photon and a phonon. This process can be used to excite the motion of the mechanical oscillator. Furthermore, the photon-phonon pairs that get created will exhibit quantum correlations, so the interaction provides a way of generating entangled states of the mechanical motion and the optical field.

Chapter 3

Multimode Optomechanics

In the previous chapter, we described the basic optomechanical system consisting of one optical and one mechanical mode. By adding more modes to the system, we can extend its capabilities and carry out more complex operations. For example, these multimode systems can be used to perform sympathetic cooling [8], microwave-to-optical photon conversion [19] or the transfer of a motional state between two mechanical modes through topological operations [20, 21] or adiabatic evolution [22]. For our study of decoherence, state transfer is of particular importance due to its application in macroscopic non-classical experiments [23], which we discuss more in depth in chapter 8.

In the first two sections of this chapter we focus on how a multimode optomechanical system can be used to transfer a motional state between mechanical modes. We describe two different mechanisms to achieve this goal, and present an experimental demonstration of each. The first, taken from our work in [24], involves the exchange of mechanical energy through two-photon processes mediated by a cavity. The second, based on our work in [25], relies on the adiabatic transformation of one of the system's eigenmodes from one mechanical mode into another. This mechanism is also mediated by the cavity, but the cavity mode is never populated.

The third section of the chapter gives a summary of our theoretical exploration of a multi-membrane optomechanical cavity, published in [18]. In addition to being an appropriate setup to implement mechanical state transfer schemes, such a system can exhibit an enhancement of the optomechanical coupling and it permits the manipulation of collective mechanical states by virtue of having more than one mechanical element.

3.1 Two-tone swapping

Consider an optomechanical system with one optical cavity mode $\hat{a}$ and two nondegenerate mechanical modes $\hat{b}_1$ and $\hat{b}_2$, which can pertain to distinct mechanical elements or can be normal modes of the same structure. Let ω_c, Ω_1 and Ω_2 be the frequency of the cavity and two mechanical modes, respectively. Furthermore, let g_{01} and g_{02} denote the single-photon optomechanical coupling rates of mechanical mode 1 and 2. The Hamiltonian of this system is the same as the optomechanical Hamiltonian we introduced in section 2.4, except now there are energy and interaction terms for each mechanical mode

$$H = \hbar\omega_c \hat{a}^\dagger \hat{a} + \sum_{j=1}^{2} \left(\hbar\Omega_j \hat{b}_j^\dagger \hat{b}_j + \hbar g_{0j} \hat{a}^\dagger \hat{a} (\hat{b}_j + \hat{b}_j^\dagger) \right) . \tag{3.1}$$

Evidently, the mechanical modes are not directly coupled to each other, but we can exploit the cavity mode to mediate an interaction between them. We now discuss two schemes in which such an interaction is used to transfer states between the mechanical modes.

Before we proceed, it will be useful to simplify the Hamiltonian as we did in section 2.4. We follow the derivation in [26] to linearize the interaction terms, and we move to a frame rotating at the cavity mode frequency by applying the unitary operator $\hat{U}(t) =$

$\exp(i\omega_c \hat{a}^\dagger \hat{a} t)$, which yields

$$H = \sum_{j=1}^{2} \left(\hbar\Omega_j \hat{b}_j^\dagger \hat{b}_j + \hbar g_{0j} (\alpha \hat{a}^\dagger e^{i\omega_c t} + \alpha^* \hat{a} e^{-i\omega_c t})(\hat{b}_j + \hat{b}_j^\dagger) \right). \tag{3.2}$$

Both of the transfer schemes that we will discuss rely on driving the cavity with a bichromatic pump that has frequency components ω_1 and ω_2. Such a drive results in an average cavity mode amplitude

$$\alpha(t) = \alpha_1 e^{-i\omega_1 t} + \alpha_2 e^{-i\omega_2 t}, \tag{3.3}$$

where the amplitudes α_1 and α_2 are chosen to be real without loss of generality. With the bichromatic pump, the Hamiltonian becomes

$$H = H_m + \sum_{j,k=1}^{2} \hbar g_{0j} \alpha_k (\hat{a}^\dagger e^{i\Delta_k t} + \hat{a} e^{-i\Delta_k t})(\hat{b}_j + \hat{b}_j^\dagger), \tag{3.4}$$

$$H_m = \sum_{j=1}^{2} \hbar\Omega_j \hat{b}_j^\dagger \hat{b}_j, \tag{3.5}$$

where we have introduced $\Delta_j = \omega_c - \omega_j$ as the detuning of the jth pump tone[1].

We can trace the cavity field out of 3.4 and derive an effective master equation for the mechanical modes [26]. This derivation is rather long, and here we present only the end result. In essence, the bichromatic pump creates a beat note inside the cavity that forms a time-dependent optical spring between the mechanical modes. Let us arbitrarily assume that $\omega_2 > \omega_1$ and $\Omega_2 > \Omega_1$. When the frequencies of the pump tones satisfy

$$\omega_2 - \omega_1 = \Omega_2 - \Omega_1, \tag{3.6}$$

---

[1] Note that this definition for the detuning is reversed from the one we employed in section 2.4

that is, when the difference in pump frequencies matches the mechanical frequency separation, the beat note resonantly couples the mechanical modes. Under the rotating wave approximation (RWA), this results in an effective interaction of the form

$$H_{int} = J(\hat{b}_1^\dagger \hat{b}_2 + \hat{b}_1 \hat{b}_2^\dagger). \tag{3.7}$$

This is a beamsplitter interaction that can be used to transfer states between the mechanical modes at an exchange rate J. The physical process responsible for the beamsplitter interaction can also be understood by looking at the relative detuning of the sidebands of the two pump tones, shown in Fig. 3.1. In the current multimode configuration, the motion of each mechanical mode will generate two sidebands on each pump tone, resulting in a total of 8 sidebands. When condition 3.6 is met, two pairs of sidebands will have matching frequencies, leading to an enhancement of two-photon processes that exchange energy between mechanical modes. For example, tone 1 will have a sideband at $\omega_1 + \Omega_2$ with photons that have been upconverted by absorbing a phonon from mechanical mode 2. Because $\omega_1 + \Omega_2 = \omega_2 + \Omega_1$, said photons can also be resonantly downconverted to match the frequency of tone 2 by creating a phonon in mechanical mode 1. A similar analysis can be done for the other pair of matched sidebands.

Note that condition 3.6 does not depend on the absolute detuning of the pump tones with respect to the the cavity resonance. This is not the case for the exchange rate J and total mechanical energy decay rate Γ, which incorporate the traced out dynamics of the cavity field. Letting $\bar{\Delta} = \frac{\Delta_1+\Delta_2}{2}$ denote the average pump detuning and $\bar{\Omega} = \frac{\Omega_1+\Omega_2}{2}$ the average mechanical frequency, we have

$$J = 2g_{01}g_{02}\sqrt{n_1 n_2}\left(\frac{\bar{\Omega}-\bar{\Delta}}{\kappa^2/4+(\bar{\Omega}-\bar{\Delta})^2} - \frac{\bar{\Omega}+\bar{\Delta}}{\kappa^2/4+(\bar{\Omega}+\bar{\Delta})^2}\right), \tag{3.8}$$

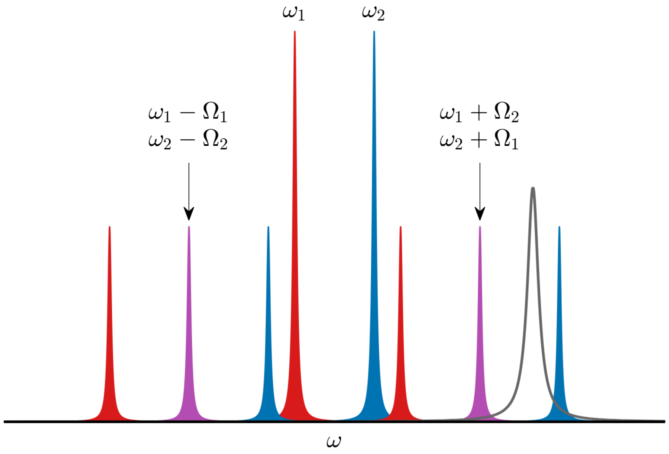

Figure 3.1: A schematic of the frequency detuning of the two pump tones and their sidebands. When the condition for the beamsplitter interaction is met, the two pairs of sidebands indicated by arrows line up, leading to energy transfer between mechanical modes. The cavity mode is shown in grey.

Mode	$\Omega/2\pi$ (MHz)	$\gamma/2\pi$ (Hz)	$g_0/2\pi$ (Hz)
1	0.25	0.183	1.0
2	0.35	0.183	1.0
3	1.15	0.096	1.5
4	1.25	0.096	1.5

Table 3.1: Experimental parameters of several mechanical modes in an optomechanical system.

$$\Gamma = \gamma_1 + \gamma_2 + \sum_{j,k=1}^{2} \frac{n_j g_{0k}^2 \kappa}{\kappa^2/4 + (\Delta_j - \Omega_k)^2} - \frac{n_j g_{0k}^2 \kappa}{\kappa^2/4 + (\Delta_j + \Omega_k)^2}, \tag{3.9}$$

where κ, γ_1 and γ_2 are the bare optical and mechanical decay rates, and n_j is the number of intracavity photons generated by the jth pump tone, as described in chapter 2. We briefly mention that J is not fully independent of Γ, and expression 3.8 is an approximation. However, in order to achieve a high transfer efficiency, we work in the regime where $J > \Gamma$, in which the approximation is valid. A complete treatment of the exact exchange rate can be found in [24, 26].

In table 3.1 we list realistic parameters of some of the modes of our membrane devices. In Fig. 3.2 we couple different pairs of these modes and plot J and Γ as a function of $\bar{\Delta}$.

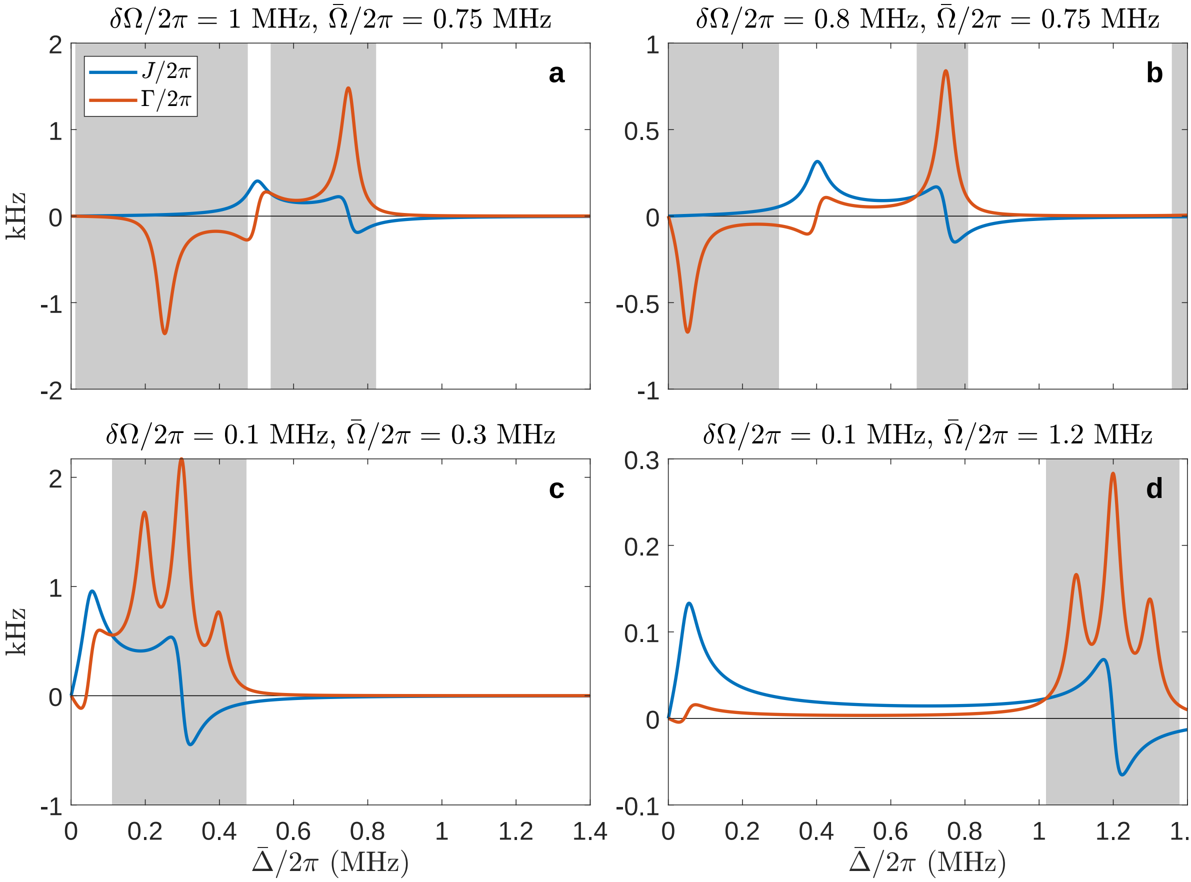

Figure 3.2: Exchange and total mechanical decay rates vs. average pump detuning. In the grey shaded regions $|J| < |\Gamma|$ and coherent state transfer is not possible. The total pump power, evenly split between both tones, is $100\,\mu$W, the cavity mode has $\kappa = 2\pi \times 50$ kHz, and the mechanical mode parameters are listed in table 3.1. The coupled modes are: (a) 1-4, (b) 2-3, (c) 1-2, (d) 3-4.

For this scheme, the sign of J has no physical significance, while a negative Γ signifies anti-damping, which is also detrimental to the transfer. Notice that the panels in the figure look quite distinct from each other, yet the only significant variation between them is the frequency separation $\delta\Omega$ and the average frequency $\bar{\Omega}$ of the coupled mechanical modes. The relationship between the rates J and Γ and the parameters $\delta\Omega$ and $\bar{\Omega}$ is complex, because it is the result of how the 8 optomechanical sidebands line up with the cavity resonance (see Fig. 3.1). Nevertheless, a rough trend can be observed. Keeping all other parameters the same, for a pair of modes that are closer in frequency or that have a higher average frequency, there will be a wider detuning range where the condition $J > \Gamma$ is satisfied and coherent state transfer can occur, at the expense of a slower exchange rate overall. Conversely, for a pair of modes with a larger frequency mismatch or lower average frequency, faster exchange rates will be possible, but coherent state transfer will only be possible over a narrower detuning range, making the feasibility of the transfer protocol less robust against frequency jitter in the pump tones.

Using this scheme, we have been able to demonstrate coherent energy transfer in the classical regime between the modes of separate mechanical resonators, achieving an exchange rate in the order of a few Hz [24], (see Fig. 3.3). The employed mechanical modes pertained to two distinct silicon nitride trampoline resonators, fabricated on opposite sides of a silicon chip. We give a picture and a more detailed description of these devices in section 5.3.2. The exchange rates measured in this proof-of-principle experiment were to a large extent limited by the fact that the cavity linewidth was large ($\kappa/2\pi = 200$ kHz), making it necessary to perform the transfer at a large average detuning in order to avoid strong optical damping. By reducing the cavity decay, it becomes possible to operate at smaller detunings where exchange rates fast enough for practical applications can be achieved. The scheme can also be extended to the quantum regime, but in order to observe coherent swapping it is necessary to minimize not just Γ, but rather its individual terms, thus reducing all sources of noise.

3.2 STIRAP

An alternative state transfer scheme relies on the process of stimulated Raman adiabatic passage (STIRAP). Consider the same Hamiltonian in Eqn. 3.4. By expanding the product of operators and moving into the interaction picture (as in section 2.4), we

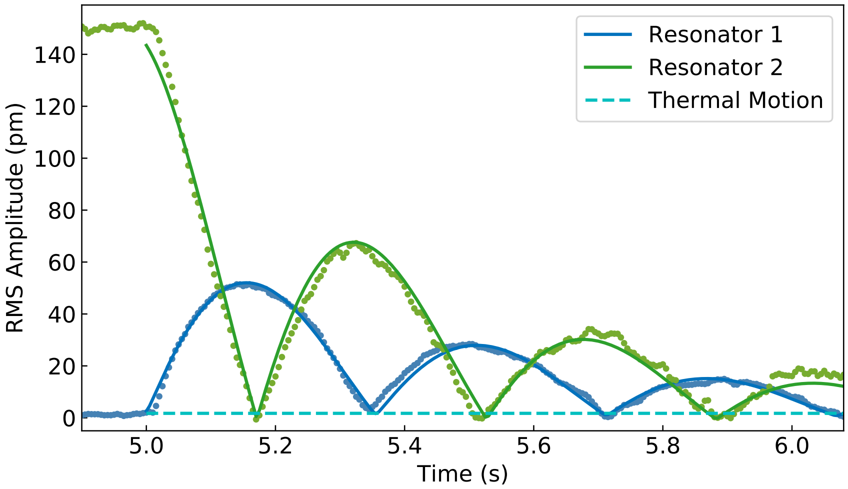

Figure 3.3: Measurement of the amplitude of motion of two resonators during a two-tone mechanical state transfer. Here, we excite resonator 2 electrostatically before we turn on the swapping interaction. Back and forth coherent oscillations can be observed, with an exchange rate of about 3 Hz. The observed decay is the result of mechanical and optomechanical damping. Figure adapted from [24].

obtain

$$H = \sum_{j,k=1}^{2} \hbar g_{0j}\alpha_k \left(\hat{a}^\dagger \hat{b}_j e^{i(\Delta_k-\Omega_j)t} + \hat{a}\hat{b}_j^\dagger e^{-i(\Delta_k-\Omega_j)t} + \hat{a}^\dagger \hat{b}_j^\dagger e^{i(\Delta_k+\Omega_j)t} + \hat{a}\hat{b}_j e^{-i(\Delta_k+\Omega_j)t}\right) \tag{3.10}$$

If each of the pump detunings is set to match one of the mechanical frequencies ($\Delta_1 = \Omega_1$, $\Delta_2 = \Omega_2$), under the RWA the Hamiltonian reduces to

$$H = \sum_{j=1}^{2} \hbar g_j (\hat{a}^\dagger \hat{b}_j + \hat{a}\hat{b}_j^\dagger), \tag{3.11}$$

where $g_j = g_{0j}\alpha_j$ are multi-photon coupling rates. In this case, each of the pump tones effectively couples the cavity to only one mechanical mode. The modes of the system can be cast into a vector $\psi(t) = [\hat{b}_1, \hat{a}, \hat{b}_2]^T$ that evolves according to Heisenberg's equation of motion [27]

$$\frac{d\psi}{dt} = \frac{i}{\hbar}[H,\psi] = i \begin{pmatrix} 0 & g_1 & 0 \\ g_1 & 0 & g_2 \\ 0 & g_2 & 0 \end{pmatrix} \psi \, . \tag{3.12}$$

The three instantaneous eigenmodes for this system are

$$\Phi_+(t) = \frac{1}{\sqrt{2}}[\sin\theta\,\hat{b}_1,\, \hat{a},\, \cos\theta\,\hat{b}_2]^T, \tag{3.13}$$

$$\Phi_-(t) = \frac{1}{\sqrt{2}}[\sin\theta\,\hat{b}_1,\, -\hat{a},\, \cos\theta\,\hat{b}_2]^T, \tag{3.14}$$

$$\Phi_0(t) = [\cos\theta\,\hat{b}_1,\, 0,\, -\sin\theta\,\hat{b}_2]^T, \tag{3.15}$$

with the mixing angle given by $\tan\theta = g_1/g_2$. The STIRAP scheme relies on the fact that eigenmode Φ_0 is a linear combination of only the mechanical modes [22]. This so-called dark mode is equal to one of the bare mechanical modes when $\theta = 0$ or $\pi/2$. Then, to perform a state transfer we can initialize Φ_0 as one of the modes and adiabatically "rotate" it into the other one by varying the mixing angle. Because Φ_0 is purely of mechanical nature, the cavity is never populated and optical losses are completely avoided. This is perhaps the most important advantage of STIRAP, since optical decay is usually the dominant loss channel in many systems.

The control over θ is possible because g_1 and g_2 can be tuned independently by adjusting the power of the corresponding pump tone. To transfer a state from $\hat{b}_1$ to $\hat{b}_2$ for example, we need to begin with $\theta(t) = 0$, $g_1(t)/g_2(t) = 0$ and end at a later time with $\theta(t+\tau) = \pi/2$, $g_1(t+\tau)/g_2(t+\tau) = \infty$. In order to remain in the dark mode, however, the transition must be slow enough. This is quantified by the adiabaticity condition

$$|\dot{\theta}(t)| = \frac{|\dot{g}_1(t)g_2(t) - \dot{g}_2(t)g_1(t)|}{g_1(t)^2 + g_2(t)^2} \ll \sqrt{g_1(t)^2 + g_2(t)^2}, \tag{3.16}$$

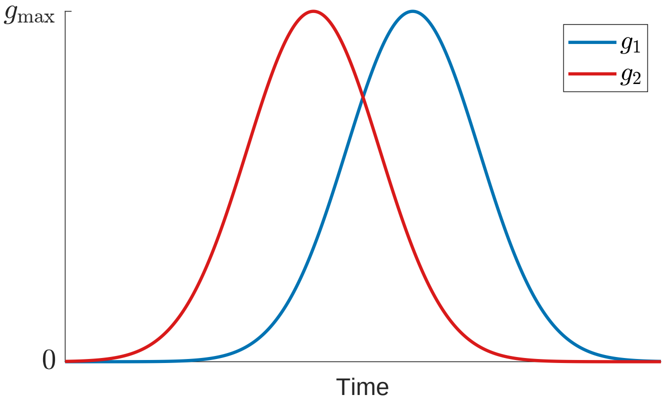

Figure 3.4: Pulse sequence to perform a state transfer using STIRAP. With the shown ordering of the pulses, a state will be transferred from mode 1 to mode 2.

where the dot represents differentiation with respect to time. A simple way to implement the scheme is by pumping the cavity with two Gaussian pulses that are offset in time, such that the time profile of the coupling rates is also Gaussian, as shown in Fig. 3.4. Then, for wide enough pulses, the adiabaticity condition can always be satisfied. In practice, the pulses cannot be arbitrarily long because the state still suffers from mechanical loss. An important detail is that the pulses must be ordered in time such that the target mode is coupled to the cavity before the mode whose state is to be transferred. This ordering might seem counterintuitive, but the reverse ordering will result in bright STIRAP, which is in general susceptible to optical losses [22]. Another notable property of STIRAP is that the time asymmetry of the scheme makes the transfer unidirectional. This nonreciprocity feature has also been demonstrated in optomechanical state transfer based on topological operations [20, 21], and allows for the possibility of fabricating components such as isolators and circulators.

We have been able to implement STIRAP for the transfer of a classical mechanical state between two modes of a silicon nitride phononic crystal membrane [25]. We discuss in more detail the mechanical device and its modes in sections 5.2.1 and 5.4. In this experiment we coupled a defect mode with the (3,3) membrane mode, shown in the left

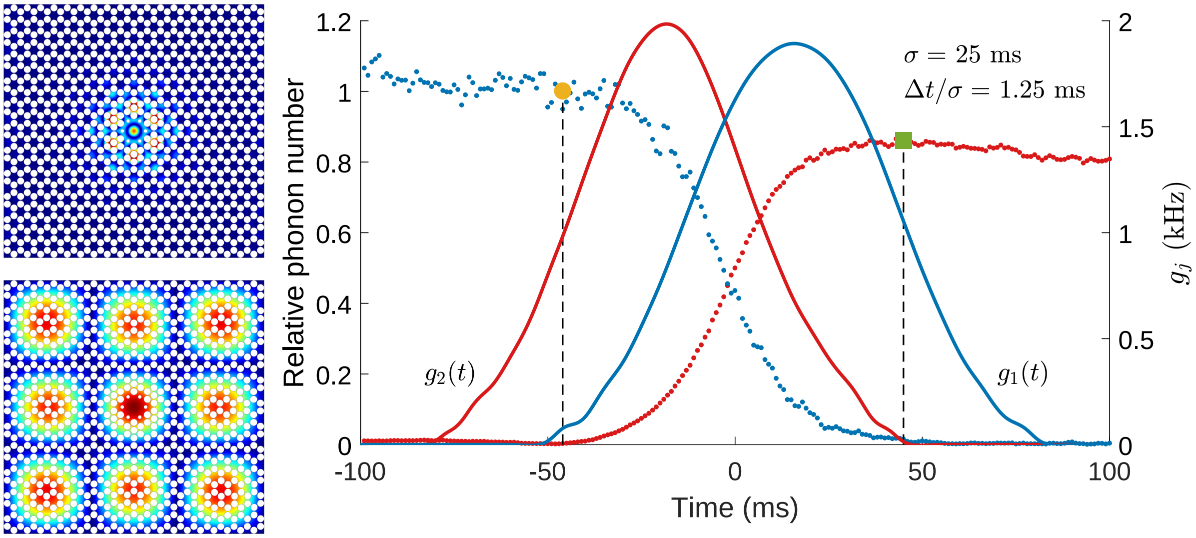

Figure 3.5: Measurement of a STIRAP state transfer. (left) Modes coupled during the transfer: mode 1, a defect mode confined to the central region of the phononic crystal; mode 2, the (3,3) mode of the entire square membrane. (right) The blue (red) dots show the phonon number in mode 1 (2), relative to the phonon number in mode 1 at beginning of the transfer (yellow circle). The solid lines represent the corresponding multi-photon coupling rates. The transfer duration is the time interval between the two dashed lines. The pulse width σ and pulse separation Δt are shown in the plot. Figure adapted from [25].

panels of Fig. 3.5. The parameters of the system were: $\omega_1/2\pi = 1.25$ MHz, $\omega_2/2\pi = 220$ kHz, $\gamma_1/2\pi = 0.096$ Hz, $\gamma_1/2\pi = 0.183$ Hz, $g_{01}/2\pi = 1.5$ Hz, $g_{02}/2\pi = 1.0$ Hz, $\kappa/2\pi = 54$ kHz. The experiment attained a transfer efficiency of 86% with an effective transfer duration τ of roughly 90 ms. This is portrayed in the right panel of Fig. 3.5, where the phonon number and coupling rate of each mode is plotted as a function of time.

In our experiment, the transfer efficiency is limited on two fronts. On the one hand, if the pulses are very long, we lose our state through mechanical decay and optical damping from the sidebands that we ignored when we performed the RWA. On the other hand, if the pulses are too short, the adiabaticity condition is not strongly satisfied, the cavity mode becomes populated, and there is subsequent optical decay. Therefore, we are forced to use a pulse width for which the combined effect of all loss channels is minimized.

The best way to improve the efficiency of the transfer is to increase the single-photon optomechanical rate of the mechanical modes, which will allow us to shorten the width of the pulses and decrease loss from mechanical decay. A more comprehensive treatment of the losses in STIRAP, including the transfer degradation that results when the pump detunings do not exactly satisfy $\Delta_1 = \Omega_1$, $\Delta_2 = \Omega_2$, can be found in [22, 25]. To conclude this section, we also mention that this scheme can be applied to couple two optical modes using an intermediary mechanical mode, as discussed in [28, 29].

3.3 Multi-membrane systems

A natural extension to the membrane-in-the-middle configuration of an optomechanical system is the use of multiple membranes [30]. Not only does such a system provide a good platform to implement the transfer schemes discussed in the previous section, but it can also exhibit an enhanced optomechanical coupling rate, and it enables the coupling of a cavity mode to collective modes of motion. Optomechanical systems with collective mechanical modes have been proposed as a platform to study optomechanical entanglement, enhanced displacement sensitivity, and optomechanical nonlinearities, among others [31].

To describe the coupling rate enhancement, we will take as an example the simplest multi-membrane system, i.e., a cavity with two membranes. As we mentioned in section 2.3.1, a membrane's wavelength-scale positioning inside a cavity determines the ratio of the field intensities on either side of it. Because the total intracavity power is fixed, a membrane's coupling rate will be largest when the cavity region with higher field intensity is made as short as possible. Then, for a system with two membranes placed near the center of the cavity, the optimal arrangement will have a maximal ratio of intensities across each membrane, with the high intensity region between them [18]. A sketch of

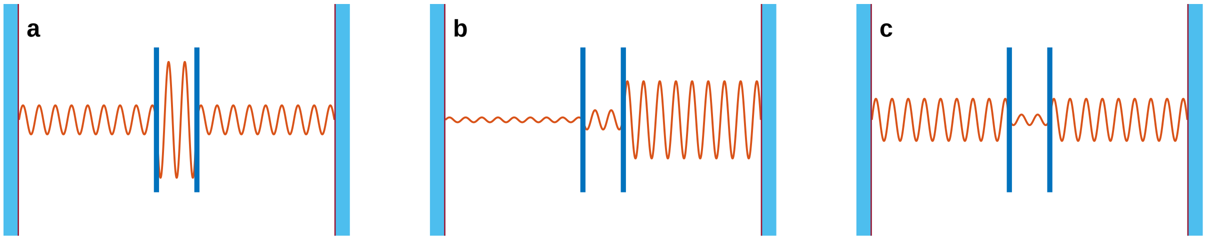

Figure 3.6: Possible configurations for two membranes near the center of a cavity. The ratio of field intensities across all membranes is the same and has been maximized. The configuration in (a) will yield maximum coupling since a big portion of the field is concentrated in the short central region, resulting in large intensity differentials across the membranes.

this configuration is shown in Fig. 3.6.

In essence, the coupling enhancement occurs because the membranes confine the field to a shorter length, which leads to a larger imbalance of radiation pressure between the two sides of each membrane. This effect can be augmented by adding even more membranes, and the optomechanical coupling rate can increase by more than an order of magnitude for the innermost membranes in the array. Fig. 3.7 shows this effect for an array of 8 membranes with a varying amplitude reflection coefficient r. If we keep increasing the number of membranes, the cavity field will become more and more confined within the array, up to the point where the field is fully contained by the membranes and the enhancement effect saturates. The number of membranes necessary to achieve saturation is not very large. Depending on their reflection coefficient, between 4 and 12 membranes will suffice.

The coupling enhancement is unfortunately accompanied by an increase in the cavity decay rate. This is because the increase in field intensity around a membrane that is responsible for the coupling enhancement also leads to an increase in absorption. The coupling rate and the absorption loss both grow linearly with the intensity of the field. Consequently, the presented enhancement scheme cannot be employed to reach the single-photon strong coupling regime. In spite of this, a multi-membrane system can still gain

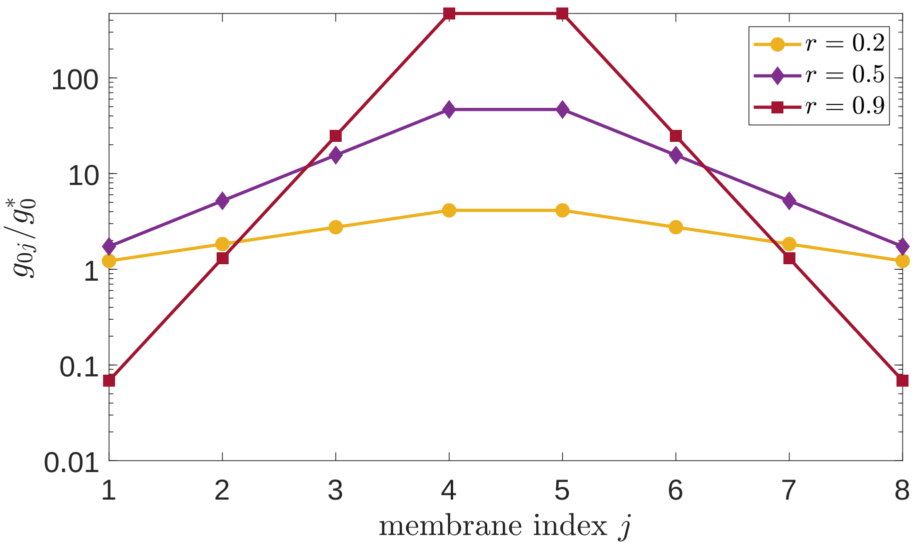

Figure 3.7: Optomechanical coupling rates for an 8 membrane array. The amplitude reflection coefficient r is shown in the legend. The individual coupling rates g_{0j} are normalized by g_0^*, the maximum coupling rate a single membrane can attain when placed near the center of the cavity.

in terms of its cooperativity, which, as discussed in section 2, determines the strength of optomechanically induced transparency, as well as the effectiveness of optomechanical cooling.

The multi-membrane systems that we have discussed also support collective mechanical modes. A pair of membranes, for example, displays a "center-of-mass" mode where the membranes oscillate in phase, and a "breathing" mode where they oscillate 180° out of phase. For the symmetric configurations shown in panels (a) and (c) of Fig. 3.6, only the breathing mode couples to the cavity field. In general, the optomechanical coupling rate of a collective mode of N membranes is given by

$$g_{0c} = \sqrt{\sum_{j=1}^{N} g_{0j}^2}, \tag{3.17}$$

where g_{0j} is the individual coupling rate of the jth membrane. Evidently, the collective coupling rate can also be enhanced by tuning the position of the membranes. Any collective mode that couples to the cavity field is described by the same optomechanical Hamiltonian from section 2.4 and can be manipulated with the same optomechanical effects, for example, optomechanical cooling [30]. A collective mode can prove useful in macroscopic superposition experiments by allowing us to prepare states that involve a larger amount of mass.

Chapter 4

Periodic Structures for Light and Motion

Here we present a brief mathematical background useful for the study of periodic structures, such as the phononic and photonic crystals that we will describe in sections 5.4 and 6, respectively. We focus on the properties of rectangular and hexagonal lattices because they are sufficient to describe the devices presented in this work. A more general and complete description of these topics, within the context of electronic and thermal properties of crystalline solids, can be found in solid-state books such as [32, 33]. The first section of the chapter is somewhat elementary, but we include it for completeness and to provide the average reader with some background.

4.1 Crystal structure

The performance of the devices that we employ in our optomechanics experiments can be dramatically improved by incorporating periodic structures into them. Such structures can be described by the same formalism used for the study of crystalline solids whose constituents are arranged in an ordered, regular fashion. At the center of this description, lies the concept of a Bravais lattice.

4.1.1 The Bravais lattice

A 2D Bravais lattice, or **lattice** for short, is a geometric arrangement of points in space, defined by two **basis vectors**, $\mathbf{a}_1$ and $\mathbf{a}_2$. The lattice is composed of all the points whose positions are given by the vectors $\mathbf{R} = m\mathbf{a}_1 + n\mathbf{a}_2$, where m and n are integers. The parallelogram generated by the basis vectors is called the **unit cell**. All of space can be spanned if we translate the unit cell by all lattice vectors $\mathbf{R}$. For a given lattice, a unit cell is called **primitive** if no other unit cell with smaller area exists which can reproduce the periodicity of the lattice.

As a first example, consider the **rectangular lattice**, which is defined by two orthogonal basis vectors of unequal magnitude. We can choose to align the basis vectors with the axes of a Cartesian plane and express them as $\mathbf{a}_1 = a_1\,\hat{\mathbf{x}}$, $\mathbf{a}_2 = a_2\,\hat{\mathbf{y}}$. The quantities a_1 and a_2 are called the **lattice constants**. A variation of the rectangular lattice is obtained by adding a lattice point at the center of each unit cell, and it is called a **centered rectangular lattice**. The left and middle panels of Fig. 4.1 shows examples of both simple and centered rectangular lattices.

Another lattice type is the **hexagonal lattice** (also named triangular lattice), and it is defined by two basis vectors of equal magnitude enclosing a 120° angle. Here, we choose the following representation $\mathbf{a}_1 = a/2\left(\hat{\mathbf{x}} + \sqrt{3}\hat{\mathbf{y}}\right)$, $\mathbf{a}_2 = a/2\left(\hat{\mathbf{x}} - \sqrt{3}\hat{\mathbf{y}}\right)$. Notice that the hexagonal lattice only has one lattice constant a. A hexagonal lattice is shown in the right panel of Fig. 4.1.

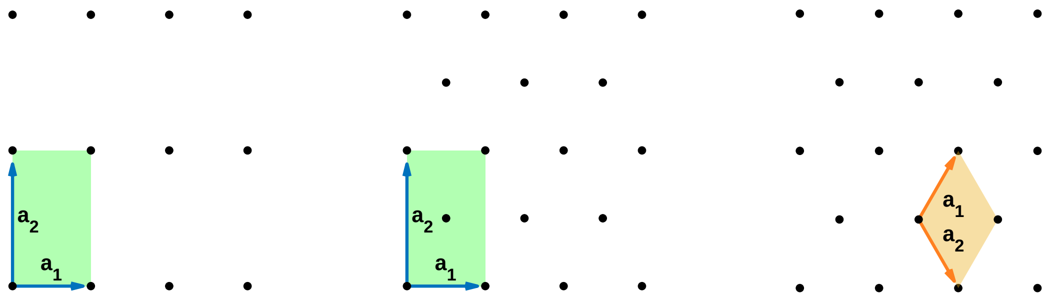

Figure 4.1: (left) A simple rectangular lattice. The shaded area denotes the unit cell. (middle) A centered rectangular lattice. The shaded unit cell is not a primitive cell. (right) A hexagonal lattice with its unit cell shaded in orange.

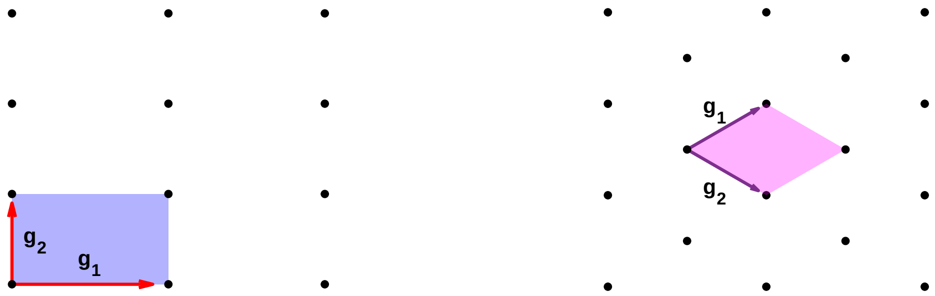

Figure 4.2: (left) The reciprocal lattice of a rectangular lattice. (right) The reciprocal lattice of a hexagonal lattice.

4.1.2 The reciprocal lattice

For any lattice, there exists a corresponding **reciprocal lattice**, and it is spanned by the **reciprocal basis vectors**, $\mathbf{g}_1$ and $\mathbf{g}_2$, which are defined by the relationship $\mathbf{g}_i \cdot \mathbf{a}_j = \delta_{ij} 2\pi$. Using the basis vector definitions from the previous section, for the case of a rectangular lattice, the reciprocal lattice vectors are simply $\mathbf{g}_1 = 2\pi/a_1\,\hat{\mathbf{x}}$, $\mathbf{g}_2 = 2\pi/a_2\,\hat{\mathbf{y}}$. The resulting reciprocal lattice is also a rectangular lattice.

For a hexagonal lattice, the reciprocal basis vectors are $\mathbf{g}_1 = 2\pi/a\left(\hat{\mathbf{x}} + 1/\sqrt{3}\hat{\mathbf{y}}\right)$, $\mathbf{g}_2 = 2\pi/a\left(\hat{\mathbf{x}} - 1/\sqrt{3}\hat{\mathbf{y}}\right)$. The reciprocal lattice is also a hexagonal lattice, except it has the orientation of the hexagons rotated by 30° with respect to the real space lattice. Fig. 4.2 depicts both a rectangular and a hexagonal reciprocal lattice.

In analogy to the real space lattice, the reciprocal lattice consists of all the points given by the vectors $\mathbf{G} = h\mathbf{g}_1 + l\mathbf{g}_2$, where h and l are integers. The units of the reciprocal basis vectors are inverse length or spatial frequency, and we say that the reciprocal lattice exists in momentum or **k-space**. Each point in the reciprocal lattice represents the wave vector of a plane wave with the same periodicity as the real space lattice. Furthermore, any function that is periodic over the real space lattice can be expanded with a Fourier series using only plane waves with wave vectors from the reciprocal lattice.

4.2 Bloch modes and the irreducible Brillouin zone

Not surprisingly, the modes of periodic structures posses special properties related to the discrete translational symmetry of the structure. This is generally true, regardless of whether the mode is optical, mechanical or of a different nature. Such modes are called **Bloch modes**, and they have the following mathematical form

$$f_{\mathbf{k}}(\mathbf{r}) = e^{i\mathbf{k}\cdot\mathbf{r}} u_{\mathbf{k}}(\mathbf{r})\,. \tag{4.1}$$

Here $u_{\mathbf{k}}$ is a periodic function sharing the same periodicity as the structure, that is, $u_{\mathbf{k}}(\mathbf{r}) = u_{\mathbf{k}}(\mathbf{r} + \mathbf{R})$. Consequently, Bloch modes can be regarded as modulated plane waves. As discussed in section 4.1.2, the periodicity of $u_{\mathbf{k}}$ allows us to expand it in a Fourier series using the reciprocal lattice vectors, and the Bloch mode can be recast as

$$f_{\mathbf{k}} = \sum_{\mathbf{G}} C_{\mathbf{k}-\mathbf{G}} e^{-i\mathbf{G}\cdot\mathbf{r}} e^{i\mathbf{k}\cdot\mathbf{r}}, \tag{4.2}$$

with the coefficients $C_{\mathbf{k}-\mathbf{G}}$ determined by Fourier analysis. Bloch modes have the property that if we shift their wave vector $\mathbf{k}$ by $\mathbf{G}$, we recover the same mode [33]. Because of this, we only need a small portion of k-space to describe all of the distinct modes of a periodic structure. This portion receives the name of first **Brillouin zone**, and it

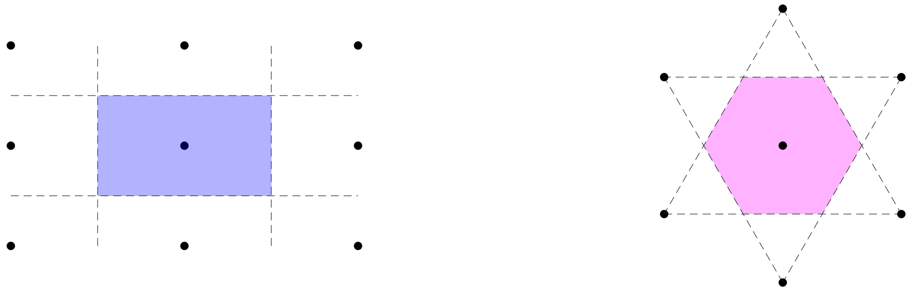

Figure 4.3: First Brillouin zone of the rectangular and hexagonal lattices.

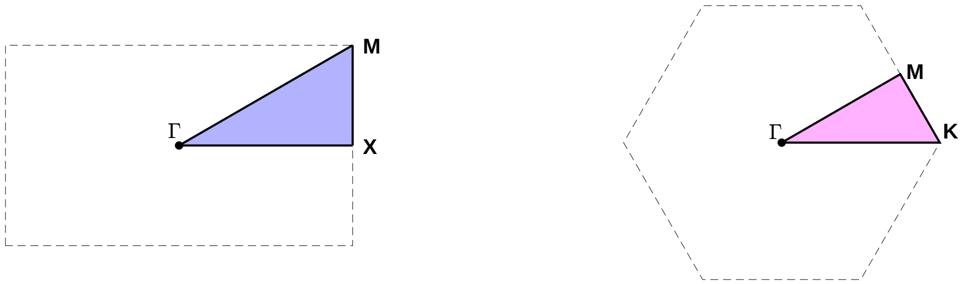

Figure 4.4: Irreducible Brillouin zone of the rectangular and hexagonal lattices, with their corresponding points of high symmetry labeled as per convention.

corresponds to a **Wigner-Seitz cell** of the reciprocal lattice, which is a type of primitive cell, constructed from all the points in k-space that are closest to any single reciprocal lattice point, as can be seen in Fig. 4.3.

Mirror and rotational symmetries of the real space lattice result in further redundancy in the Brillouin zone, which allows us to focus on an even smaller section called the **irreducible Brillouin zone** (IBZ). Certain points of high symmetry in the IBZ receive special names set by convention [34]. The IBZ of the rectangular and hexagonal lattices and their corresponding high-symmetry points are shown in Fig. 4.4. For reference, the coordinates of the symmetry points are listed in table 4.1.

Rectangular lattice			**Hexagonal lattice**		
	$\mathbf{g}_1$	$\mathbf{g}_2$		$\mathbf{g}_1$	$\mathbf{g}_2$
Γ	0	0	Γ	0	0
X	1/2	0	K	1/3	1/3
M	1/2	1/2	M	1/2	0

Table 4.1: Coordinates of the symmetry points of rectangular and hexagonal lattices, in terms of their respective reciprocal lattice vectors.

4.3 Band structure

By computing the Bloch modes of the periodic structure at different points in the irreducible Brillouin zone, we can obtain the mode frequencies as a function of wave vector. As we sweep the Brillouin zone, each mode traces a curve called a **band**, each of which is part of the full **band structure** of the system. Certain systems have band structures with frequency ranges were no band is present, which receive the name of **bandgaps**. Within these bandgaps there can be no energy propagation because no mode exists at the corresponding frequencies to transport energy. Bandgaps give rise to interesting phenomena with many useful applications, such as LED's, superprisms, Bragg mirrors, photonic crystal waveguides and fibres, to name a few. Another application of bandgaps in periodic structures is phononic shielding, which we explore in section 5.4. Because the extrema of the bands normally occur at one of the high symmetry points, calculating the bands along the edge of the irreducible Brillouin zone is usually sufficient to extract key features of the band structure, such as the existence of bandgaps and their corresponding widths and midgap frequencies.

4.4 Link between hexagonal and rectangular lattices

A relationship exists between the hexagonal and rectangular lattices. The particular case of a centered rectangular lattice with $a_2/a_1 = \sqrt{3}$ is equivalent to a hexagonal

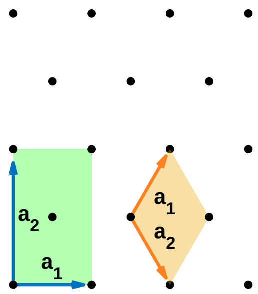

Figure 4.5: A rectangular lattice with $a_2/a_1 = \sqrt{3}$, which can also be regarded as a hexagonal lattice with lattice constant $a = a_1$. Both shaded regions are unit cells of the lattice, but only the hexagonal cell is a primitive cell.

lattice with $a = a_1$, as shown in Fig. 4.5. This equivalence is useful when carrying out numerical computations to study structures with hexagonal periodicity, since some important numerical methods, such as FDTD (see appendix A), only support rectangular simulation regions.

When representing a hexagonal lattice as a centered rectangular lattice, the unit cell is no longer a primitive cell. In real space, the rectangular unit cell has twice the area of the primitive hexagonal cell. As a result, the rectangular Brillouin zone has half the area of the hexagonal Brillouin zone. Still, since the rectangular cell is a valid unit cell of the lattice, the rectangular Brillouin zone must contain all the distinct modes of the structure. This means that every point in the rectangular Brillouin zone corresponds to two distinct points of the related hexagonal Brillouin zone. We say then, that the hexagonal Brillouin zone is folded onto the rectangular one. This can be seen schematically in Fig. 4.6.

Band folding can make the results of band structure calculations hard to interpret, and although unfolding procedures can be carried out [35], it is usually more practical to calculate band structures with methods that support non-rectangular simulation regions, such as FEM (see appendix A). Nevertheless, as mentioned previously, rectangular cell representations of hexagonal structures are of practical importance when carrying out FDTD simulations, which are a fast method to obtain the broadband response of a

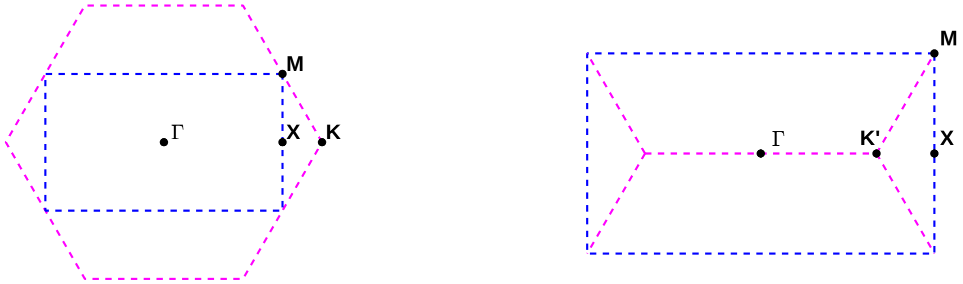

Figure 4.6: (left) Two possible Brillouin zones for a structure with hexagonal symmetry, each corresponding to one of the unit cells shown in Fig. 4.5. (right) The hexagonal zone has been folded onto the rectangular one along its edges. The K-point has been mapped to a new point K′.

periodic structure and can help provide insight into a problem by solving it in the time domain.

Chapter 5

Thin Membranes

In chapters 2 and 3 we discussed optomechanical systems in the membrane-in-the-middle configuration and some of their applications. We now focus on the properties of the membranes themselves. We begin this chapter by introducing the theory of linear elasticity used to study the mechanical modes of solids. Next, we present a quantitative model for the mechanical modes of a clamped membrane, followed by a description of sources of energy loss and ways to mitigate them. The last section of the chapter is concerned with the properties of phononic crystals and their application towards reducing the dissipation of energy in the mechanical modes of a membrane.

5.1 Theory of elasticity

To study the mechanics of a solid body, such as a membrane, we employ the theory of elasticity [36, 37]. The variable of interest is the **displacement field** $\mathbf{u}(x, y, z, t)$ which quantifies the magnitude and direction of the displacement of each point of the body from some initial position. The evolution of $\mathbf{u}$ in time is governed by Newton's second law of motion, which can be stated as

$$\rho \frac{\partial^2 \mathbf{u}}{\partial t^2} = \nabla \cdot \sigma + f, \tag{5.1}$$

where ρ is the mass density, σ is the second-rank **stress tensor**, and f is any external force per volume acting on the body. The elements σ_{ij} $(i, j = \{x, y, z\})$ refer to a force per area along i acting on a face normal to j of a volume element inside the body, and they quantify all the normal and shear stresses that result from deformations. To characterize these deformations we employ the second-rank **strain tensor** ε, which gives a description of changes in volume and shape. Being second-rank tensors in 3 dimensions, σ and ε are composed of 9 elements. However, both σ and ε are symmetric as a result of conservation of angular momentum ($\sigma_{ij} = \sigma_{ji}$, $\varepsilon_{ij} = \varepsilon_{ji}$), which means they each only contain 6 independent elements.

We are mainly interested in the dynamics of the solid under small strains, far from the regime of plastic (permanent) deformation. In this case, we can restrict ourselves to a linear elastic treatment. Then, the stress is related to the strain by a linear constitutive equation, which is a generalization of Hooke's law for continuous media

$$\sigma = C : \varepsilon, \tag{5.2}$$

where C is the fourth-rank **stiffness tensor** and the operator $:$ represents a tensor double dot product ($A : B = \sum_{i,j} A_{ij} B_{ij}$). Evidently, the stiffness tensor encodes the relation between the magnitude and direction of a deformation of the body and the resulting restoring forces. Being a fourth-rank tensor, C has 81 entries C_{ijkl}, however, symmetry considerations bring down the number of independent elements to 21 for the general case of a fully anisotropic material. On the other hand, for an isotropic material, C contains only 2 independent elements, and Eq.5.2 can be greatly simplified as

$$\sigma = \frac{E\nu}{(1+\nu)(1-2\nu)}\mathrm{tr}(\varepsilon)I + \frac{E}{1+\nu}\varepsilon, \tag{5.3}$$

where tr(·) is the trace and I is the second-rank identity tensor, while **Poisson's ratio** ν and **Young's modulus** E are material parameters that are obtained empirically.

Under our small strain assumption, we can write the strain tensor in terms of the displacement field

$$\varepsilon = \frac{1}{2}\left(\nabla\mathbf{u} + (\nabla\mathbf{u})^T\right). \tag{5.4}$$

Notice that $\nabla\mathbf{u}$ is a second-rank tensor with elements $\nabla\mathbf{u}_{ij} = \partial u_i/\partial j$, where $i,j = \{x,y,z\}$. Using Eqs. 5.3 and 5.4 we can recast the equation of motion 5.1 into a partial differential equation for the displacement field

$$\frac{E}{2(1+\nu)}\left(\nabla^2\mathbf{u} + \frac{1}{1-2\nu}\nabla(\nabla\cdot\mathbf{u})\right) + f = \rho\frac{\partial^2\mathbf{u}}{\partial t^2}. \tag{5.5}$$

This equation fully describes the motion of an isotropic linear elastic material. Lastly, we introduce an expression for the strain energy U of the body, which will be useful in the discussion of bending losses

$$U = \frac{1}{2}\int \sigma : \varepsilon\, dV. \tag{5.6}$$

5.2 Vibrations of a thin plate

In what follows, we will treat the equation of motion for a plate of finite thickness. Before we proceed, a clarification of nomenclature is in order. In the literature, a **plate** is defined as a structure that has one dimension much smaller than the other two [38]. A

membrane also fulfills this condition, but is additionally defined as having no bending stiffness, and can be seen as the limiting case of an infinitely thin plate, in analogy to a string being the limiting case of an infinitely thin beam. Then, strictly speaking, the devices we fabricate and use in our experiments are actually thin plates with a small but non-zero resistance to bending. In this section, we will make a distinction between a plate and an ideal membrane to emphasize the characteristics that arise from having a non-zero thickness. However, for simplicity, in subsequent sections we will revert to referring to real devices as membranes.

Although Eq. 5.5 is generally valid under the assumptions presented in the previous section, it can normally only be solved numerically (see appendix A). We can simplify Eq. 5.5 for the case of a thin plate, which will yield useful insight into the dynamics. Consider a plate of thickness d that extends in the xy-plane, with its top and bottom surfaces normal to the z-axis and its midplane located at $z = 0$. Because the plate is thin, the vertical displacement (along the z-direction) will be largely independent of z, that is

$$u_z(x, y, z) \approx w(x, y), \tag{5.7}$$

where we have renamed the z-component of the displacement field as w for convenience. Furthermore, the plate can easily bend when a small stress is applied on its surface, and the resulting internal stresses from elongation or compression will be much larger. Therefore, we can set to zero the components of the stress acting on faces normal to the z-axis:

$$\sigma_{xz} = \sigma_{yz} = \sigma_{zz} = 0. \tag{5.8}$$

We can combine Eqs. 5.7 and 5.8 with 5.3 and 5.4 to obtain the full strain tensor in terms of w:

$$\varepsilon_{xx} = -z\frac{\partial^2 w}{\partial x^2}, \quad \varepsilon_{yy} = -z\frac{\partial^2 w}{\partial y^2}, \quad \varepsilon_{xy} = -z\frac{\partial^2 w}{\partial x \partial y}, \quad \varepsilon_{zz} = \frac{-\nu}{1-\nu}(\varepsilon_{xx} + \varepsilon_{yy}), \tag{5.9}$$

and $\varepsilon_{xz} = \varepsilon_{yz} = 0$. By using Eqs. 5.3 and 5.8 with 5.6 we find that the strain energy of the plate is given by

$$U = \int \frac{E}{1+\nu}\left[\frac{(\varepsilon_{xx}+\varepsilon_{yy})^2}{2(1-\nu)} - \varepsilon_{xx}\varepsilon_{yy} + \varepsilon_{xy}^2\right] dV. \tag{5.10}$$

If we assume the material properties are constant throughout the plate, the strain energy becomes

$$U = \frac{Ed^3}{12(1+\nu)} \iint \left[\frac{1}{2(1-\nu)}\left(\frac{\partial^2 w}{\partial x^2} + \frac{\partial^2 w}{\partial y^2}\right)^2 - \frac{\partial^2 w}{\partial x^2}\frac{\partial^2 w}{\partial y^2} + \left(\frac{\partial^2 w}{\partial x \partial y}\right)^2\right] dx\, dy. \tag{5.11}$$

Then, by employing a variational approach to minimize the strain energy of the system [36], we obtain the following equation of motion for w

$$-\frac{D}{d}\nabla^4 w + f = \rho\frac{\partial^2 w}{\partial t^2}, \tag{5.12}$$

where $D = \frac{Ed^3}{12(1-\nu^2)}$ is the flexural rigidity of the plate [38], and f is any external force per volume acting on the plate. We can model the important case of a plate under a uniform tensile prestress S by calculating the restoring forces f that arise from the in-plane tension as the plate vibrates. These can be obtained from geometrical considerations [39] and plugged into Eq. 5.12, yielding

$$-\frac{D}{d}\nabla^4 w + S\,\nabla^2 w = \rho\frac{\partial^2 w}{\partial t^2}. \tag{5.13}$$

We note that in Eqs. 5.12 and 5.13, the gradient operator ∇ acts only on the in-plane coordinates x and y. At this point, it should be apparent that we have effectively reduced the problem to two dimensions, by virtue of one of the dimensions of the plate being much smaller than the other two.

5.2.1 Vibrational modes

Equation 5.13 closely resembles the wave equation in two dimensions, so it should not be surprising to find that it is satisfied by sinusoidal functions. We are interested in the case of a square plate of side length L that is clamped around its boundary: $w(0, y) = w(x, 0) = w(L, y) = w(x, L) = 0$. Assuming harmonic oscillations in time, the solutions take the form

$$w(x, y, t) = e^{-i\omega_{mn}t} \sin(k_x x) \sin(k_y y), \tag{5.14}$$

with $k_x = \frac{m\pi}{L}$, $k_y = \frac{n\pi}{L}$ and $m, n = \{1, 2, 3, ...\}$ in order to satisfy the boundary conditions. We plot some of the solutions in Fig. 5.1. By plugging the mode functions 5.14 into Eq. 5.13, we obtain the mode frequencies

$$\omega_{mn} = \frac{\pi}{L\sqrt{\rho}} \sqrt{S(m^2 + n^2) + \frac{D\pi^2}{hL^2}(m^4 + 2m^2n^2 + n^4)}. \tag{5.15}$$

We notice that there are two contributions to the mode frequencies. The first arises from the external prestress S, and the second from the internal stresses that result from bending. Evidently, if we set the flexural rigidity of the plate to zero, or equivalently, if we make the plate infinitely thin, we recover the dispersion relation of an ideal membrane with a wave propagation speed $c = \sqrt{S/\rho}$. The devices we employ are made of high-stress silicon nitride with $S \approx 800$ MPa, $E = 270$ GPa and $\nu = 0.27$. For our typical device dimensions of $d \sim 50$ nm and $L \sim 3$ mm, a quick calculation shows that the external prestress will be the dominant contribution to the restoring forces driving the plate's motion by roughly a factor of $\frac{S}{E}\left(\frac{L}{d}\right)^2 \approx 10^9$.

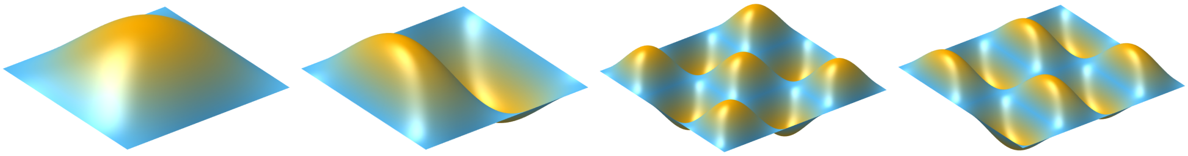

Figure 5.1: Vibrational modes of a thin plate. From left to right, the mode indices (m, n) are $(1, 1)$, $(2, 1)$, $(3, 3)$ and $(4, 2)$.

We note that in a real clamped plate, the modes are never exactly sinusoidal, as this would require an infinite amount of bending at the edges of the plate. A more accurate description of the modes treats them as sinusoidal throughout the bulk of the plate, but with quadratic tails near the edges [40]. This description is necessary to properly quantify bending losses at the clamp points of the structure. Nevertheless, the model we have presented for the mode shapes and frequencies is useful for most practical purposes.

As a final remark, we mention that the discussion we have presented for the motion of a plate can be easily "collapsed" into a 1D model for the study of structures such as thin beams, tethers and cantilevers. This is also the case for the loss models that we discuss in the following section.

5.3 Dissipation of mechanical energy

So far we have described a model for mechanical modes in a membrane with no dissipation. In practice of course, the mechanical quality factor of the modes is not infinite, since mechanical energy gets dissipated through multiple decay channels.

5.3.1 Bending losses

As the membrane vibrates, some of its energy is stored as bending energy, which is quantified by Eqs. 5.10 and 5.11. We observe that the bending energy depends on the curvature of the mode and on the material's Young modulus. Bending losses are modeled by adding to the Young modulus an imaginary component E_l known as the **loss modulus** ($E \rightarrow E + iE_l$). The loss modulus is responsible for an inelastic dissipation of energy during each cycle as a result of bending, quantified by

$$\Delta U = 2\pi \int \frac{E_l(x,y)}{1+\nu} \left[\frac{(\varepsilon_{xx} + \varepsilon_{yy})^2}{2(1-\nu)} - \varepsilon_{xx}\varepsilon_{yy} + \varepsilon_{xy}^2 \right] dV. \tag{5.16}$$

The physical origin of E_l has been largely attributed to material defects, modeled as two-level systems (TLS) whose energy splitting is modulated as a result of the oscillating strain. Such a modulation is believed to result in an occupation of these TLS away from thermal equilibrium, resulting in energy dissipation in the form of heat flow [41, 42]. There is some indication that such material defects occur largely during the fabrication of the devices [41], through contamination from wet etchants, or damage caused during ion etching (see chapter 7).

For a membrane with fixed boundaries, the regions of highest curvature are at its edges and at the modes' antinodes. Consequently, the largest contribution to the bending energy loss comes from those regions. An important strategy to reduce the bending losses at the boundaries is based on the principle of **soft clamping** [43–45], which consists of making the modes gradually decay into a periodic medium where their propagation is forbidden. This avoids sharp bends at fixed edges and considerably reduces bending loss. We discuss the use of phononic crystals to implement soft clamping in section 5.4.

Even with soft clamping, a real membrane will always bend to some degree throughout the bulk as it vibrates (for example, at the antinodes). This inherent bending loss can be dramatically decreased by applying a prestress to the membrane. This occurs because as the membrane's prestress increases, a greater portion of its energy is stored as elongation energy, which is largely insensitive to the defects in the material [40, 41, 46]. We can see this quantitatively by analysing the quality factor of the mechanical modes, given by $Q = 2\pi U_T/\Delta U$, where U_T is the total mechanical energy. For a given mode, U_T can be obtained by integrating the maximum kinetic energy:

$$U_T = \frac{\omega^2}{2} \int \rho(x,y) w(x,y)^2 \, dV. \tag{5.17}$$

Using Eqs. 5.15 and 5.17 we can see that the mechanical quality factor will increase as the prestress S increases. It is thanks to this mechanism that silicon nitride structures with high prestress can display high quality factors not usually attainable in amorphous materials [47]. One can also exploit this mechanism through **stress engineering**, whereby the geometry of the structure is altered such that the stress is locally increased at regions of high curvature [45].

5.3.2 Radiation losses

Radiation of mechanical energy into the supporting structure is another important loss channel in mechanical resonators [46, 48]. As a further complication, the losses resulting from clamping depend on how the samples are held down, which can lead to the mechanical quality factors varying orders of magnitude every time a device is remounted. In order to mitigate this, we fabricated structures that are nested within a low-frequency outer oscillator. Fig. 5.2 shows a silicon nitride trampoline that is held by an outer trampoline that acts as a low-pass filter, effectively reducing the coupling of the inner higher frequency device to modes in the substrate and making it insensitive to how the chip is clamped. These devices exhibit Q's of above 10^5 at room temperature, with no variation from remounting [49].

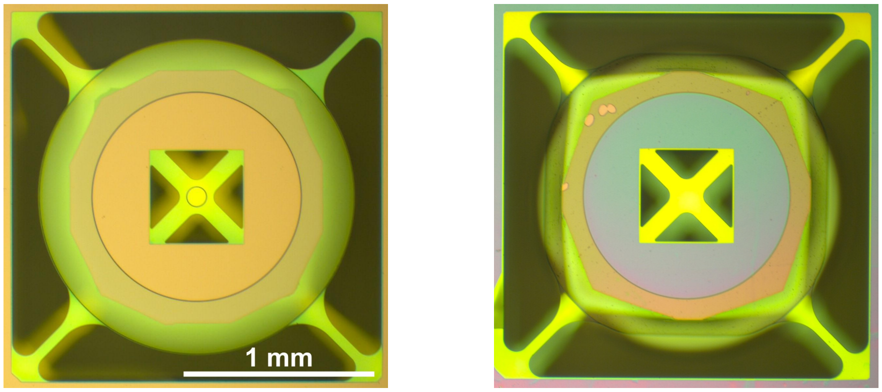

Figure 5.2: A silicon nitride nested trampoline resonator. The large, low-frequency outer trampoline acts as a low-pass filter that effectively decouples the inner trampoline from the substrate. The device has an inner trampoline on both sides. (left) Front side. The circle in the middle of the inner trampoline is a Bragg mirror. (right) Back side. The inner trampoline is identical to the one in the front, except it does not have a mirror.

Soft clamping, which we will discuss in section 5.4, is another effective way of mitigating clamping losses [44, 45], since the modes of interest do not extend all the way out to the clamping points.

5.3.3 Other loss mechanisms

Thermoelastic dissipation [50] and Akhiezer damping [51, 52] have also been investigated as potentially limiting the mechanical quality factor of silicon nitride structures. Thermoelastic damping is a direct consequence of the thermoelastic effect when a structure has a non-uniform strain field that causes temperature gradients and irreversible heat flow. For silicon nitride structures, thermoelastic losses are predicted to limit Q at around 10^{12} [48], which indicates that they are not the dominant loss source for the best devices reported with Q's between 10^8 and 10^9.

Akhiezer damping occurs when an oscillating strain field modulates the mode frequencies, causing the population of each mode to shift away from thermal equilibrium. Energy is dissipated as the modes return to equilibrium by scattering with thermal phonons. This type of damping is strongest at frequencies close to the inverse phonon relaxation time τ_{ph} which is usually on the order of picoseconds [51], and is therefore not a limiting factor for the Q of our devices with frequencies around 1 MHz.

5.4 Phononic crystals

Phononic crystals are mechanical periodic structures that support a discrete set of Bloch modes (see chapter 4). Fig. 5.3 depicts a silicon nitride membrane patterned with a 2D phononic crystal of hexagonal symmetry, along with its band structure and the shapes of the first few lowest order modes.

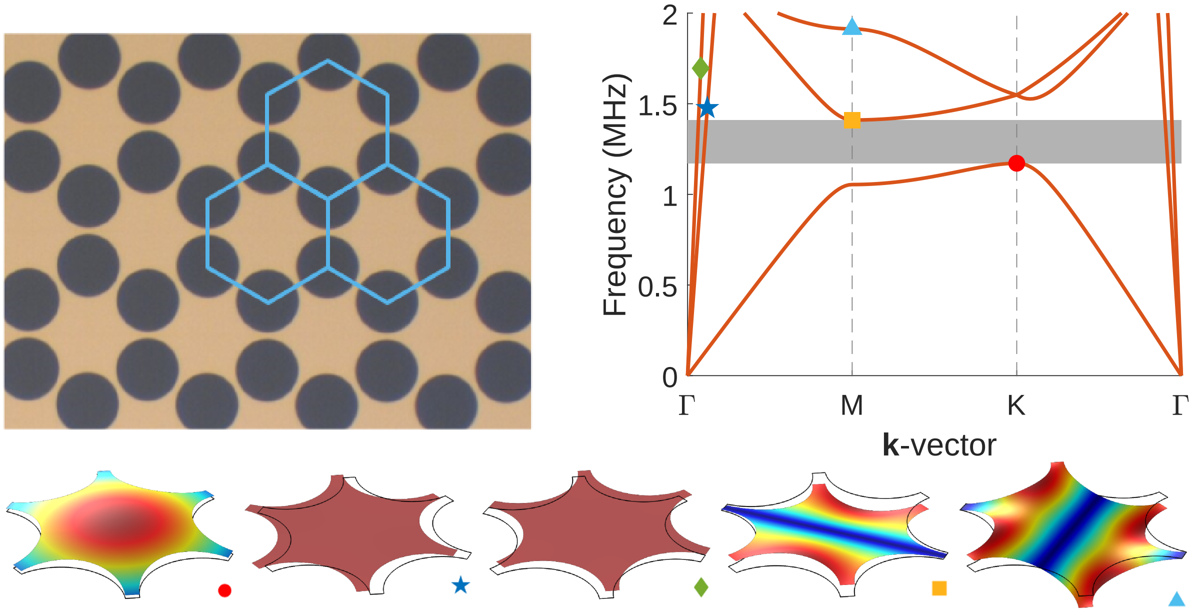

Figure 5.3: (top left) Hexagonal phononic crystal with a few unit cells marked in blue. (top right) Band structure of the crystal. The grey area shows a bandgap for out-of-plane polarized modes. (bottom) Mode shapes for the modes in the band structure plot with the corresponding symbols.

A key feature of the band structure is that there is a bandgap for transverse (out-of-plane) modes. Within the bandgap frequency range no transverse vibrations can propagate through the crystal, and we exploit this feature in order to create isolated mechanical modes. By altering the geometry around one lattice site, we form a **defect** that supports modes with frequencies that lie within the bandgap of the surrounding crystal. Fig. 5.4 shows three defect modes for a defect in the phononic crystal from Fig. 5.3.

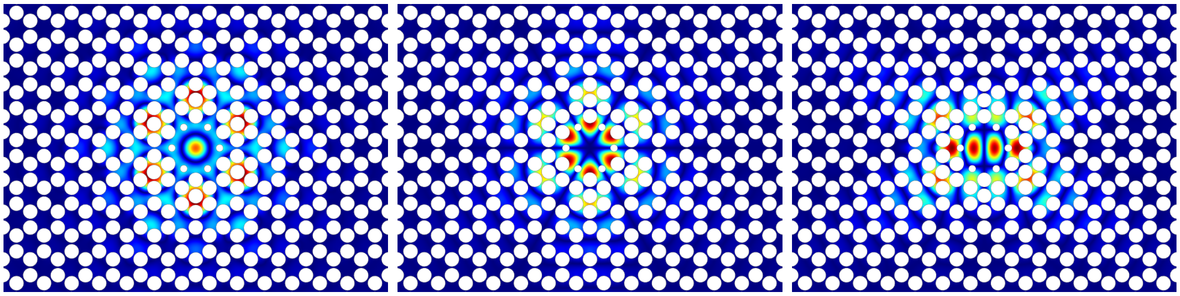

Figure 5.4: Defect modes with frequencies that lie within the bandgap of the surrounding phononic crystal. The modes cannot propagate through the crystal and are localized around the defect.

The fact that the defect mode frequencies lie within the bandgap has two important consequences. First, the defect modes are evanescent within the phononic crystal and slowly decay without any sharp bends, greatly reducing bending losses. Second, since the defect modes do not reach the clamping points, they are decoupled from all the substrate modes, which mitigates radiation losses. In this way, phononic crystals are very efficient at reducing the dominant loss mechanisms present in micro and nanomechanical resonators. The devices we fabricate consistently exhibit Q's above 10^7 at room temperature and we have measured Q's of above 10^8 at cryogenic temperatures. Other experimental groups with devices that incorporate phononic crystals report some of the highest mechanical quality factors to date [45, 53, 54].

5.4.1 Design and optimization

Patterning a phononic crystal into a prestressed membrane results in a spatially varying mass density and stress field. The lowest order membrane modes (such as those in Fig. 5.1) retain their shape and only have their frequency modified to match the new average density and stress, so they can still be approximately treated with the model from section 5.2.1. On the other hand, higher-order modes with wavelengths on the order of the lattice constant ($\lambda \sim a$) can resolve the density and stress variations and require a different treatment. This is the case for the modes of the crystal's unit cell and of the defect, which we calculate numerically using FEM (see appendix A).

In order to design a defect, one can start by lightly varying the parameters of a unit cell to tune the frequency of the desired modes into the bandgap. In our case, to arrive at the defect geometry shown in Fig. 5.4, we started from a design that had already been shown to exhibit high Q's [44] and adjusted the number, radius, and placement of the holes, while trying to minimize the bending of the membrane for the modes of interest.

The defect that we found to be optimal is shown in Fig. 5.5 and has the following geometry: starting from the unperturbed crystal, the radius of the six holes that surround the defect cell is reduced by a factor of 2. The holes are displaced to the centers of the nearest-neighbor cells and subsequently shifted towards the center of the defect by a distance equal to their radius. Finally, regular holes are added at the center of the cells that are second nearest-neighbor to the original defect cell.

5.5 Further improvements

We have already mentioned that stress engineering has the potential of further increasing the Q of membrane modes. A promising avenue to investigate is the further optimization of defect geometries in order to enhance the stress in the defect and mitigate bending losses even more. Silicon nitride has a yield strength of about 6 GPa [45], so high-stress devices with $S \approx 1$ GPa can still see a significant improvement of roughly a factor of 5.

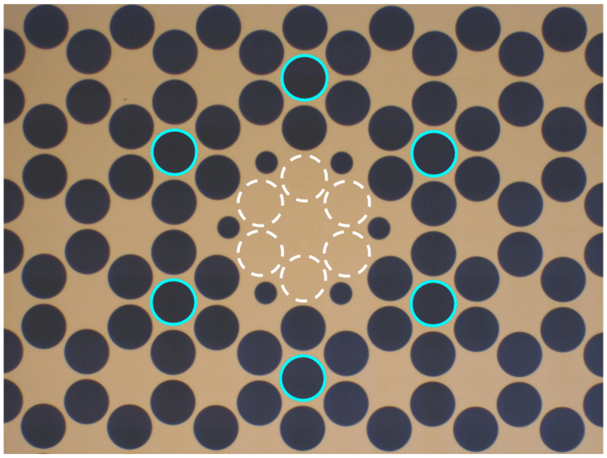

Figure 5.5: Defect in a phononic crystal membrane. The dashed circles indicate the original size and location of the small holes. The circles with solid outlines are added.

Another interesting prospect is the investigation of other materials for the fabrication of mechanical resonators. Crystalline solids are good candidates for this, since their ordered structure is associated with a smaller number of intrinsic TLS that contribute to energy loss. Indeed, phononic crystals made of single crystal silicon have displayed record Q's above 10^{10} [53]. Currently, we are working to fabricate phononic crystal membranes out of single crystal diamond.

Chapter 6

Photonic Crystal Mirrors

The use of periodic structures for the manipulation of waves is certainly not restricted to the mechanical regime. Just as the phononic crystals we presented in section 5.4 modify the energy transport of mechanical waves, periodic structures can also alter the propagation of electromagnetic waves. Such structures receive the name of **photonic crystals**. Over the past two decades, the study of photonic crystals has seen an accelerated pace due to the increasing availability of computational tools that allow for the numerical calculation of electromagnetic mode profiles and band structures, which cannot usually be calculated analytically.

Photonic crystals have several applications in the fields of optics and photonics, including low-loss optical fibers and waveguides, beam splitters, circulators, high quality factor resonators and mirrors [55–59]. In this work, we focus on photonic crystal mirrors, which can be implemented in different ways depending on the application. 1D photonic crystals, commonly known as Bragg reflectors, can be employed for fiber and free space propagation systems. They consist of a stack of alternating layers with different electric permittivity and they offer high reflectivity bands independent of the polarization and incidence angle of the incoming light [60]. However, they can only confine light along one direction, and for best performance the layers must have an optical thickness (real thickness times the refractive index of the material) on the order of a quarter wavelength, resulting in devices that extend for several microns along the propagation axis, which limits their uses. For optical modes that propagate within thin beams or slabs of dielectric material, 1- and 2D photonic crystals can act as high-reflectivity mirrors [56, 59]. A rather striking feature of 2D photonic crystals in thin dielectric slabs is that they can also exhibit arbitrarily high reflectivities for out-of-plane propagation [61]. This feature is particularly useful in membrane-in-the-middle optomechanics, where a high reflectivity of the membrane can be achieved [62, 63], enhancing the optomechanical coupling rate, while avoiding the increased mechanical losses introduced by other approaches, such as coating the membranes with metal [46].

This chapter is devoted to the study of photonic crystal slabs interacting with out-of-plane waves, as a means to increase the reflectivity of the membranes employed in our experiments. We begin with a description of the modes of a thin slab of dielectric material and later we describe the effects of embedding a periodic structure within the slab. We find that the enhanced reflectivity is the result of interference between two scattering mechanisms for the incident light.

Throughout this chapter, all of the calculations were carried out using the FDTD method, except for the design parameter optimizations in section 6.5 which were obtained with RCWA. For a short description of the employed numerical methods and tools, please refer to appendix A.

6.1 Photonic crystal slabs

A photonic crystal slab (PCS) is a structure that is periodic in two directions, but unlike a “true” 2D photonic crystal, a PCS has a finite extent in the direction perpendicular to the plane of periodicity. This has the important consequence of preventing the existence of complete bandgaps in the band structure of electromagnetic modes of the PCS. Nevertheless, a PCS can exhibit total reflection for waves propagating normally with respect to the slab. In order to understand the reflectivity enhancement of these devices, it is useful to first look at the electromagnetic modes of a bare dielectric slab.

6.1.1 Electromagnetic band structure of a thin dielectric slab

Consider a thin dielectric slab which is infinite along the xy-plane and has a thickness d along the z-axis and a refractive index $n > 1$. The wave vector $\mathbf{k}$ of any mode of the slab can be decomposed into two components $\mathbf{k}_{\parallel}$ and $\mathbf{k}_{\perp}$ which represent the components parallel and perpendicular to the plane of the slab, respectively. This can be seen schematically in Fig. 6.1.

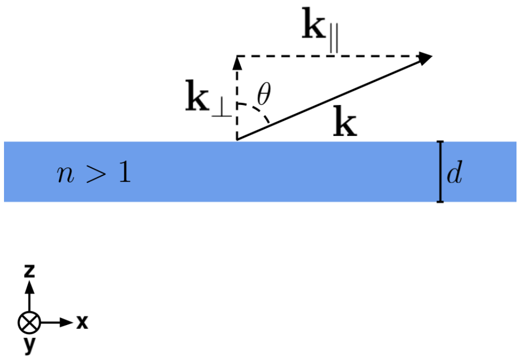

Figure 6.1: A dielectric slab extending infinitely along the x-y plane. The diagram shows the decomposition of any k-vector into in- and out-of-plane components.

Due to the continuous translational symmetry of the system, $k_{\parallel} = k \sin\theta$ is a conserved quantity for any given mode, even across the boundary between distinct media. The frequency ω is also conserved, and the **dispersion relation** $\omega = ck$ that connects $k_{\parallel}$ and ω can be plotted to visualize the band structure of the slab. For the present case of an infinite dielectric slab, the dispersion relation can be obtained analytically [64], but in this work, we solve for it numerically and plot it in Fig. 6.2.

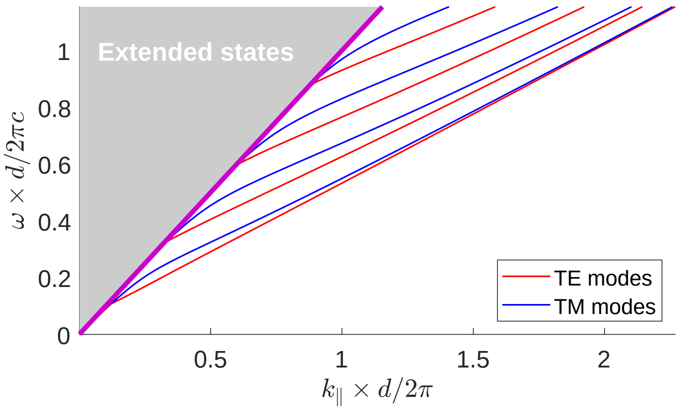

Figure 6.2: Frequency of the modes of a thin dielectric slab of thickness d, as a function of in-plane k-vector. The light line $\omega = ck_\parallel$ is shown in purple.

Here, transverse electric (TE) (transverse magnetic (TM)) modes have an electric field that is even (odd) with respect to the midplane of the slab. Let us analyze the band structure by using the dispersion relation $\omega = c\sqrt{k_\parallel^2 + k_\perp^2}$. Above the **light line** $\omega = ck_\parallel$ we find a continuum of propagating modes that extend into the air and dielectric regions. These are all plane waves with spatial dependence proportional to $e^{i\mathbf{k}\cdot\mathbf{r}}$, and they form a continuum because $k_\perp$ can take on any real value. As the waves pass from one medium to another, only their angle of propagation changes, as dictated by Snell's law of refraction (a consequence of the conservation of ω and $k_\parallel$). On the other hand, below the light line, the solutions in air must have $k_\perp$ purely imaginary, resulting in **evanescent** modes that decay exponentially away from the dielectric-air boundary and are thus confined to exist within the slab through **total internal reflection**. Such modes are said to be **index guided**, and because they are confined to a finite region of space, their spectrum is discrete. Such modes can propagate indefinitely inside the dielectric, provided there are no imperfections that break the translational symmetry of the system.

6.1.2 Band structure of a PCS and guided resonances

Consider now a PCS obtained by taking the slab from the previous section and adding a periodic arrangement of circular holes with lattice constant a and radius r, as shown in Fig. 6.3. The band structure of the PCS, calculated numerically, is shown in Fig. 6.4. We have somewhat arbitrarily chosen to work with a hexagonal lattice (for reasons discussed in section 6.5), but the presented results are equally valid for square lattices.

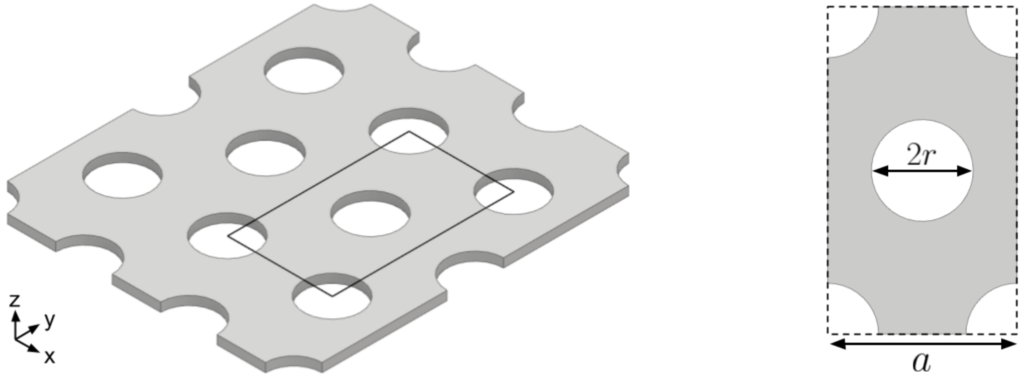

Figure 6.3: (left) A photonic crystal slab with a hexagonal lattice of holes. (right) Unit cell employed for the calculation of the band structure in Fig. 6.4.

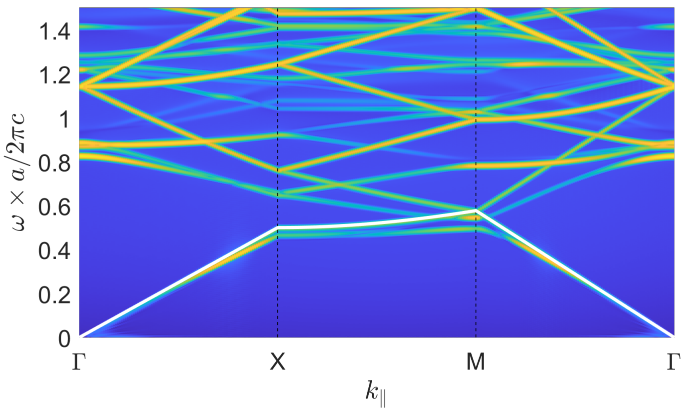

Figure 6.4: Band structure of a hexagonal PCS. Above the light line, shown in white, the modes can couple to the continuum of propagating plane waves.

The band structure of the PCS presents some important differences with regards to that of a bare dielectric slab. The discrete translational symmetry of the PCS results in $k_{\|}$

being conserved, but only to within a reciprocal lattice vector **G**. Consequently, we only need to plot the band structure in the first Brillouin zone (refer to chapter 4 for a discussion of the reciprocal lattice and the Brillouin zone). More importantly, the PCS supports modes above the light line, which have an intrinsic decay channel as a result of the coupling to the continuum of propagating modes. Consequently, any excitation of these modes will decay in time, even in a structure with no defects. Such "lossy" modes receive the name of **guided resonances**, because they still retain part of their guided nature, that is, a significant portion of their field profile is localized within the dielectric. In the following section, we will discuss how the guided resonances are responsible for the reflection enhancement of a PCS.

For the remainder of the chapter and unless otherwise specified, all the figures will refer to a PCS suspended in air, made of Si_3N_4 ($n = 2$), of thickness $d = 50$ nm and with a and r optimized for reflection at a wavelength $\lambda = 1064$ nm. These are the parameters of the devices used in our experiments.

6.2 Reflection enhancement

Photonic crystal slabs cannot exhibit complete band gaps, because modes are supported for all frequencies above the light line. Still, they can have reflectivities of 100 % for light at normal incidence. This is because, unlike the phononic shielding discussed in section 5.4, the reflectivity enhancement is an interference effect that does not rely on the existence of a bandgap. It occurs when the PCS supports a guided resonance with the same frequency and in-plane wave vector as the incident light. When this is the case, part of the incident wave is promptly reflected (or transmitted) and part of it excites the guided resonance and subsequently leaks out of the slab. Interference between these two channels results in the modified reflection and transmission of the slab. The following model for the reflection and transmission coefficients of the PCS describes the phenomenon [61],

$$r = r_e \pm f \frac{\gamma}{i(\omega - \omega_0) + \gamma}, \tag{6.1}$$

$$t = t_e + f \frac{\gamma}{i(\omega - \omega_0) + \gamma}, \tag{6.2}$$

where the sign in Eq. 6.1 is determined by whether the guided resonance is even or odd with respect to the midplane of the slab. γ and ω_0 are the linewidth and frequency of the guided resonance, and $f = -(r_e \pm t_e)$, from energy conservation arguments. The coefficients r_e and t_e describe prompt reflection and transmission from the PCS as if it were unpatterned and had an effective dielectric constant ϵ_e. This constant can be extracted by fitting the background of the reflection or transmission spectrum of the PCS to that of a uniform slab. In general, ϵ_e is frequency dependent, and at lower frequencies it approaches the average dielectric constant of the PCS.

The coefficients r_e and t_e together represent a background channel through which incident light can propagate as it interacts with the PCS (through prompt reflection or transmission, respectively). The other channel is described by the resonant term in Eqs. 6.1 and 6.2, which represents the light that excites a guided resonance and subsequently leaks out. The interference of a background and a resonant scattering process usually results in a Fano resonance [65], and this is precisely the case for the process described here, as is evident from the reflectance spectrum shown in Fig. 6.5, simulated for a linearly polarized plane wave at normal incidence.

6.2.1 Symmetry

From the model in Eq. 6.1, we should expect to see a reflection peak at the resonant frequency of every guided mode of the PCS. For radiation at normal incidence ($\theta = 0$,

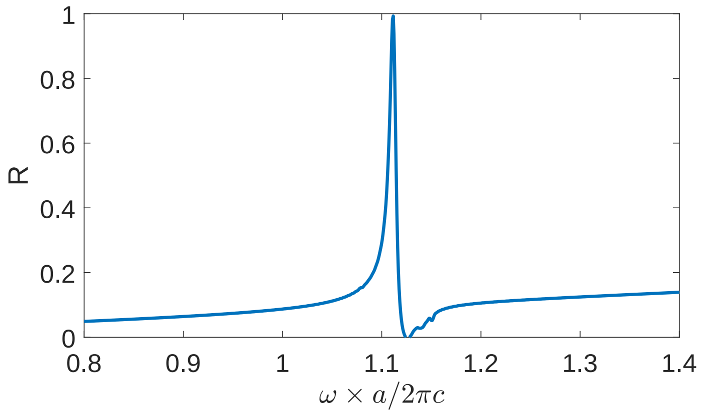

Figure 6.5: Simulated reflectance spectrum of a PCS, displaying an asymmetric Fano resonance.

$k_{\parallel} = 0$), we look at the mode frequencies at the Γ-point of the Brillouin zone (see Fig. 6.4). Within the normalized frequency range from 0.8 to 1.4, there is clearly more than one mode, yet we observe a single peak in the reflectance spectrum of Fig. 6.5. The reason why we do not observe other peaks is that the incident radiation can only excite modes with matching symmetry [66]. The spectrum in Fig. 6.5 is calculated for a plane wave at normal incidence and polarized along the x-axis. Such a field has even and odd symmetry with respect to the x and y-axis, respectively. We consider a mode as even (odd) about an axis if after reflection through said axis the field points in the same (opposite) direction. In Fig. 6.6 we show the field profile for different modes at the Γ-point, along with their corresponding symmetries. Notice that only one mode has the same symmetry of the incident plane wave. This is the only mode that gets excited and for which a reflectivity enhancement is observed.

6.2.2 Angular dependence

As discussed previously, the incident radiation and a guided resonance must have the same frequency and in-plane k-vector in order to observe a reflectivity enhancement. Because $k_{\parallel} = \frac{\omega}{c} \sin\theta$, this condition results in a reflectance spectrum that is dependent

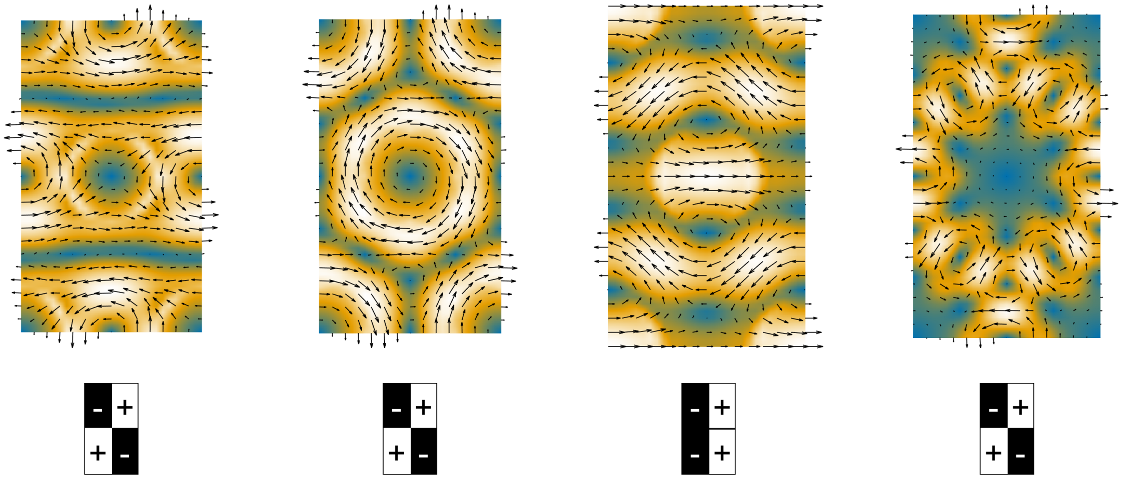

Figure 6.6: Field profile and symmetries of some the modes at the Γ-point. The arrows indicate the direction and magnitude of the field.

on the incidence angle of the radiation, as shown in Fig. 6.7.

The angular reflectance spectrum is to some extent a mapping of the band structure of the PCS. However, the connection between both pictures is slightly more complicated, because one should also consider the symmetry of the modes and the dependence of the coefficients r_e and t_e on the incidence angle. In general, modes with flatter bands as a function of $k_{||}$ will result in a large reflectivity enhancement over a broader angle range.

6.3 Performance limitations

Although the reflectivity enhancement in photonic crystal slabs can be of 100 %, it has some limitations in practice. The first limitation arises from the dependence of the PCS reflectivity on the angle of incidence. The spectra in Fig. 6.7 show that this dependence can be rather sharp, and slight deviations from normal incidence can greatly reduce the reflectivity. Even at normal incidence, the reflectivity enhancement will be limited for real light sources. As opposed to a plane wave which has a delta function spectrum in k-space, the commonly used Gaussian beam can be decomposed as a collection of plane

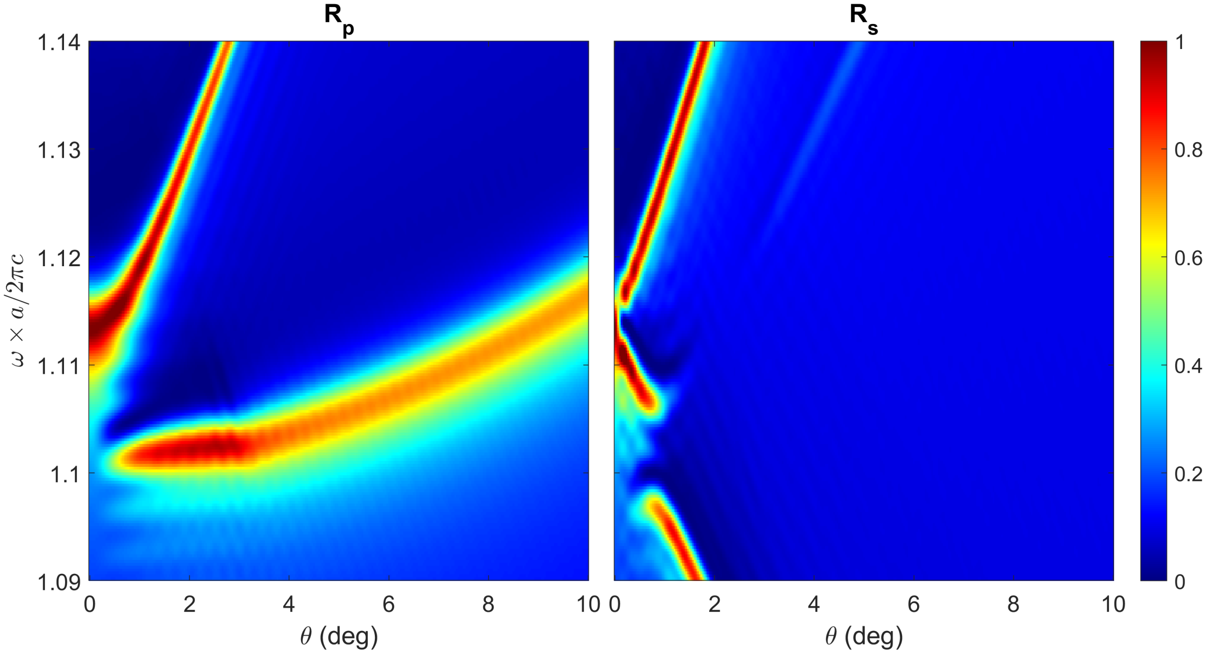

Figure 6.7: Angular reflectance spectrum of a PCS for p and s polarization.

waves with a Gaussian distribution of k-vectors, which can be recast in terms of incidence angle

$$\rho(\omega, \theta) = \frac{1}{A} \exp\left(\frac{-k_{\|}^2 w_0^2}{4}\right) = \frac{1}{A} \exp\left(\frac{-(\frac{\omega}{c}\sin\theta)^2 w_0^2}{4}\right), \tag{6.3}$$

where w_0 is the beam waist and A is a normalization constant. The width of the distribution is inversely proportional to w_0, so for tightly focused beams, a large portion of the beam's power will be contained in plane wave components with large $k_{\|}$ and thus large θ. We can calculate the reflectivity of a PCS for an incident Gaussian beam by taking the average of the angular reflectance spectrum of the PCS weighted by the angular power distribution of the beam

$$R(\omega) = \int R_p(\omega, \theta)\rho(\omega, \theta)d\theta \int R_s(\omega, \theta')\rho(\omega, \theta')d\theta'. \tag{6.4}$$

Here we have split the integral into p and s polarization contributions, since the 2-dimensional k-space distribution of the beam contains components of both kinds. We have assumed that the beam has a circular profile, but elliptical beams can be easily considered by using weight functions with different beam waists along each dimension. Fig. 6.8 shows the angular reflectance spectra of a PCS at $\omega = 2\pi c/1064$ nm, overlapped with the angular power distribution of a Gaussian beam with $w_0 = 10$ μm. It is clear that a significant portion of the beam's power is incident at a larger angle and will experience a lower reflectivity.

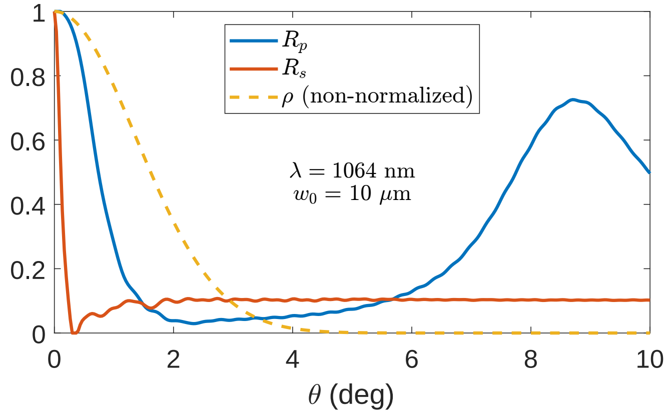

Figure 6.8: Overlap of the angular power distribution of a Gaussian beam with the angular reflectance spectra of a PCS. The dashed line represents the angular power distribution of a Gaussian beam.

In Fig. 6.9 we have plotted Eq. 6.4 as a function of w_0, over a small frequency range near $\omega = 2\pi c/1064$ nm. Evidently, for very small w_0 the reflectivity of the PCS is severely limited. As w_0 gets larger, the Gaussian beam becomes more like a plane wave, with a sharply peaked Fourier spectrum, and we recover the large reflectivity enhancement. In practice, this imposes a minimum spot size for a Gaussian beam if high reflectivity is desired.

The beam spot size must also be bounded from above in order to achieve high reflectivity with any real PCS. At its focus, a Gaussian beam has 99 % of its power contained

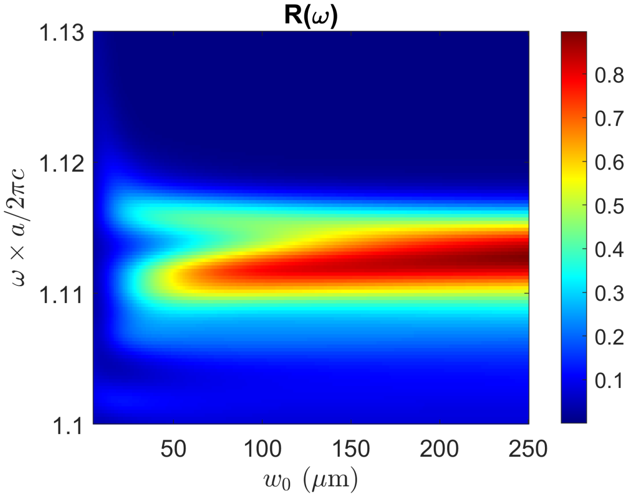

Figure 6.9: Computed reflectivity for a Gaussian beam, as a function of beam waist.

within a circle of radius 1.52 $w0$ [64]. However, even if a photonic crystal is larger than this size, the reflectivity enhancement might still be limited [67]. This is because in a PCS of finite transverse extent, light can freely propagate in-plane and escape at its edge. Recall that light in a guided resonance couples to out-of-plane propagating modes which interfere with the incident radiation and cause the reflectivity enhancement, but if the light reaches the edge of the photonic crystal too quickly this cannot occur. This can be quantified by comparing the decay rates through the two channels. First, the linewidth γ of the guided resonance, which we introduced in section 6.1.2, describes how quickly the guided resonance leaks out to the out-of-plane propagating modes. It is an intrinsic property of the guided resonance and it is determined by the geometry and dielectric properties of the PCS and the surrounding medium. The second decay rate γ_t corresponds to the loss from the in-plane propagation of the mode. To first order,

$$\gamma_t = \frac{\alpha}{w_0^2}, \tag{6.5}$$

where α is the curvature of the guided resonance's band at the Γ-point [68]. In order to have a high reflectivity, light must mostly leak out into the out-of-plane propagating modes, that is, $\gamma \gg \gamma_t$. This can be achieved more easily for larger crystals since beams with larger waists can be employed.

Next, we consider the impact of the thickness of the PCS. In general, a thicker PCS will be more robust at displaying a reflectivity enhancement, as a result of two effects. The first is that the linewidth of the guided resonances γ increases for thicker slabs as shown in Fig. 6.10. A heuristic argument for why this occurs is that as the thickness of the slab increases, the mode's profile decays more rapidly away from the dielectric-air interface, which corresponds to a broader distribution in k-space, so the resonance can couple to more propagating modes resulting in a faster decay.

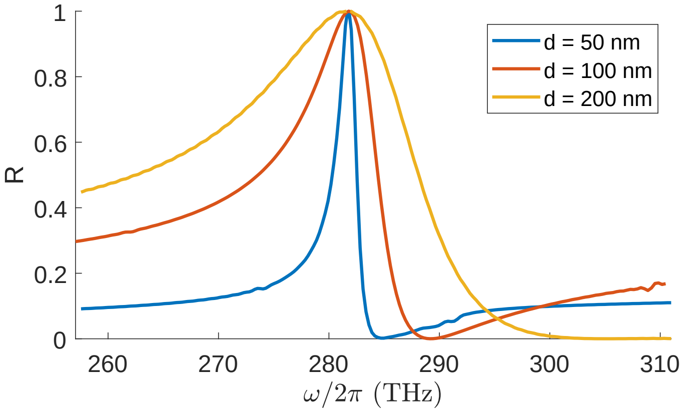

Figure 6.10: Fano resonance for various slab thicknesses. The linewidth increases for increasing slab thickness.

As γ gets larger it becomes the dominant decay channel over γ_t, enhancing the reflectivity. Since the resonances are broader, this also means that there will be a reflection enhancement over a wider frequency range. The second effect has to do with the band structure of the PCS. As the slab gets thicker, the curvature of the bands at the Γ-point decreases. This makes the angular dependence of the reflectivity less sharp (see Fig. 6.11), thus allowing for more tightly focused beams. At the same time, a reduced α reduces the transverse leakage, following Eq. 6.5. Clearly, the thickness of the PCS largely determines the performance of the device, and to achieve high reflectivity, thicker devices will be better.

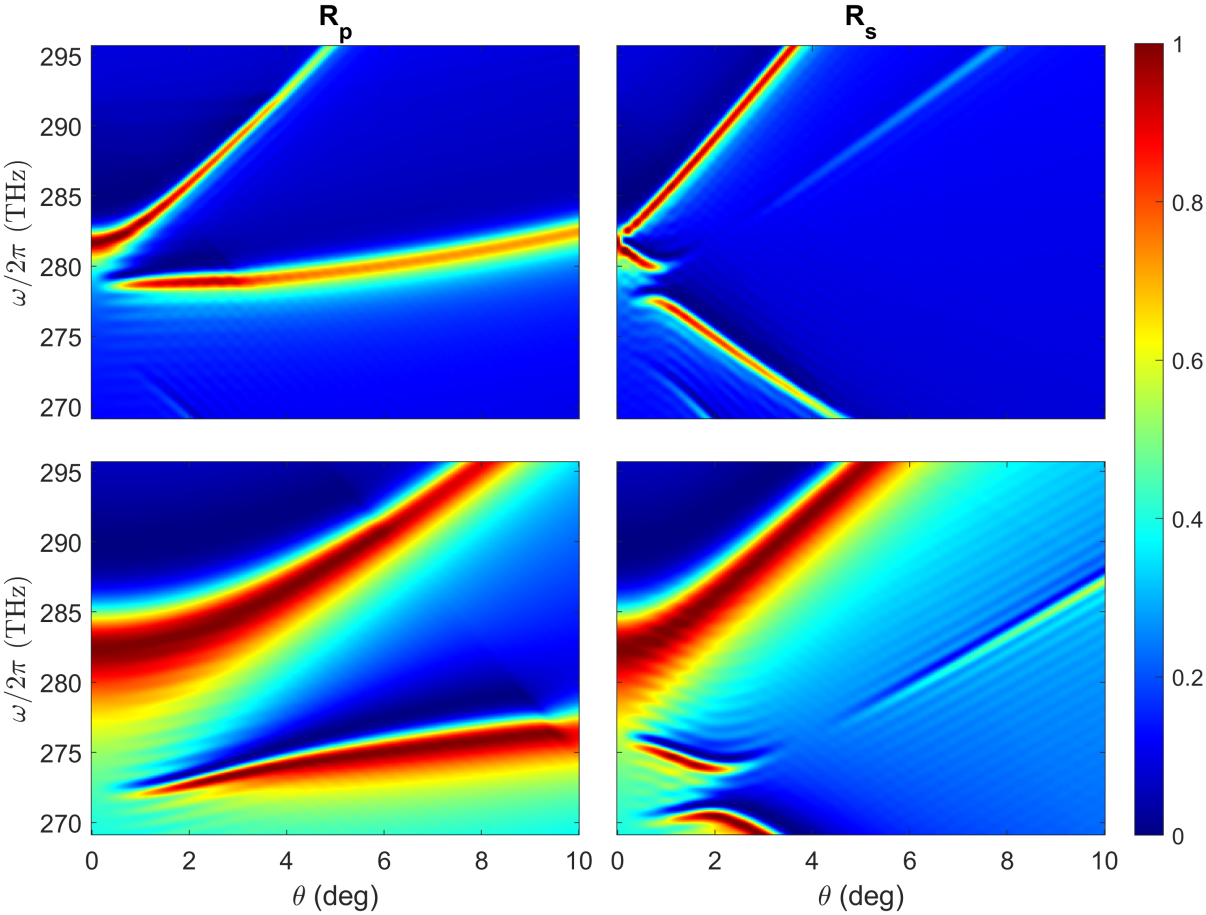

Figure 6.11: Comparison of angular reflectance spectra for different thicknesses of a PCS, (top) $d = 50$ nm, (bottom) $d = 100$ nm.

For completeness, we mention that material imperfections will also limit the performance of a PCS. Absorption in the material can be regarded as an extra decay channel for the guided resonance, with its corresponding decay rate γ_a. Just as with the case of transverse leakage, any absorption in the material will reduce the amount of light that leaks through the desired channel (out-of-plane propagating modes). On the other hand, imperfections in the photonic crystal, which may arise during the fabrication process, will spoil the discrete symmetry of the system, allowing the guided resonance to couple to undesired propagating modes that in general do not interfere to enhance the reflectivity.

6.4 Diffraction

Since PCS are periodic structures, it is appropriate to investigate if they will cause any diffraction of the incident waves. In section 6.1.2 we stated that the in-plane wave vector $\mathbf{k}_\parallel$ of the incident field is conserved only up to addition of a reciprocal lattice vector. As a result, there will be coupling to other modes whose in-plane wave vector satisfies $\mathbf{k}'_\parallel = \mathbf{k}_\parallel + \mathbf{G}$. This can result in the reflection of diffracted waves which could limit the performance of the devices by reducing their reflectivity and making them unsuitable to be placed inside a cavity. The condition for a diffracted reflection to exist, is that its out-of-plane wave vector be real, which will be the case if $|\mathbf{k}|^2 \geqslant |\mathbf{k}'_\parallel|^2$. Using the definition of reciprocal lattice vector from section 4.1.2, this inequality becomes

$$\left(\frac{2\pi}{\lambda}\right)^2 \geqslant |\mathbf{k}_\parallel|^2 + m^2|\mathbf{g}_1|^2 + n^2|\mathbf{g}_2|^2 + 2m\mathbf{k}_\parallel\cdot\mathbf{g}_1 + 2n\mathbf{k}_\parallel\cdot\mathbf{g}_2 + 2mn\mathbf{g}_1\cdot\mathbf{g}_2\,. \tag{6.6}$$

Setting $\mathbf{k}_\parallel = k_\parallel(\cos\phi\,\hat{\mathbf{x}} + \sin\phi\,\hat{\mathbf{y}})$ and using the reciprocal basis vectors of a hexagonal lattice that we also defined in section 4.1.2, Eq. 6.6 becomes

$$1 \geqslant \sin^2\theta + 2\frac{\lambda}{a}\sin\theta\left[(m+n)\cos\phi + (m-n)\frac{\sin\phi}{\sqrt{3}}\right] + \frac{4}{3}\left(\frac{\lambda}{a}\right)^2(m^2+mn+n^2)\,. \tag{6.7}$$

Evidently, the zeroth-order reflection ($m = n = 0$) will always exist, accounting for the specular reflection at an angle $-\theta$. For close to normal incidence ($\theta = 0$), only the third term on the RHS of Eq. 6.7 is relevant to determine if there will be higher-order diffracted waves. For a fixed a, the first diffraction orders that appear as we vary λ are ($m = 1$, $n = 0$) and ($m = 0$, $n = 1$). We can observe that these will occur only if $\lambda/a \leqslant \sqrt{3}/2 \sim .866$. For the design parameters we employ, this condition is never fulfilled, as can be seen in table 6.1, so we do not observe any diffracted waves.

6.5 Design

The design of a photonic crystal slab consists of finding a combination of parameters a and r that display enhanced reflectivity for a wavelength of interest, given a device thickness and refractive index. The parameters employed in the fabrication of our devices are shown in table 6.1. Using RCWA (see appendix A) we calculate the reflectivity for a plane wave as we sweep a and r. Fig. 6.12 shows the result of such a sweep for structures of varying thickness and lattice type. In all cases, we observe a reflectivity enhancement "ridge" in parameter space where $R = 1$. The optimal parameters are determined by finding a for which the peak as a function of r is widest. This approach minimizes the possible performance degradation of the PCS as a result of fabrication imperfections. In this regard, the left and middle panels in Fig. 6.12 show that for a fixed thickness, a hexagonal lattice provides an advantage over a square lattice, because it exhibits slightly wider peaks. For this reason, we have chosen to use a hexagonal lattice in our study.

d (nm)	a (nm)	r (nm)	λ/a
50	1185	319	0.898
75	1128	244	0.943
100	1096	287	0.971

Table 6.1: Design parameters for the photonic crystal slabs studied in this work. These are calculated for $n = 2$, $\lambda = 1064$ nm.

From the middle and right panels of Fig. 6.12, it is evident that for a given lattice type, a thicker PCS exhibits a broader reflection enhancement ridge. In practice, factors such as increased absorption and bending mechanical losses (see section 5.3.1) prevent us from increasing the thickness of our devices indefinitely.

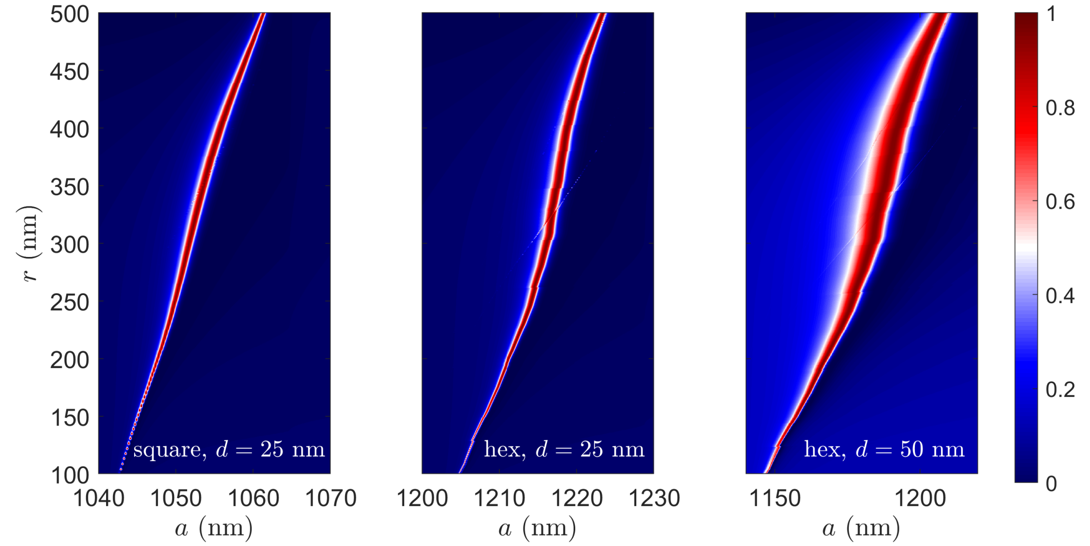

Figure 6.12: Parameter sweeps of lattice constant and hole radius, for varying thickness and lattice type. The color scale indicates the reflectivity R.

Chapter 7

Fabrication

The devices that we have discussed throughout this thesis are only a couple millimeters in size and have features that range from several microns down to a few hundred nanometers. In order to make such small devices, we must resort to the tools and techniques employed for semiconductor device fabrication. This chapter summarizes the entire fabrication process of our phono/photonic crystal membranes.

7.1 Fabrication process

The entire fabrication process is represented schematically in Fig. 7.1. An explanation of each of the panels is provided in the following sections.

(a-b) Deposition of high-stress silicon nitride on initial substrate

The fabrication process begins with a (100)-oriented silicon wafer that has a nominal thickness of 525 μm. An external company deposits on both sides of the wafer a layer of stoichiometric silicon nitride, out of which the membranes will be patterned. The amount of nitride that is deposited is determined by the desired membrane thickness. We have

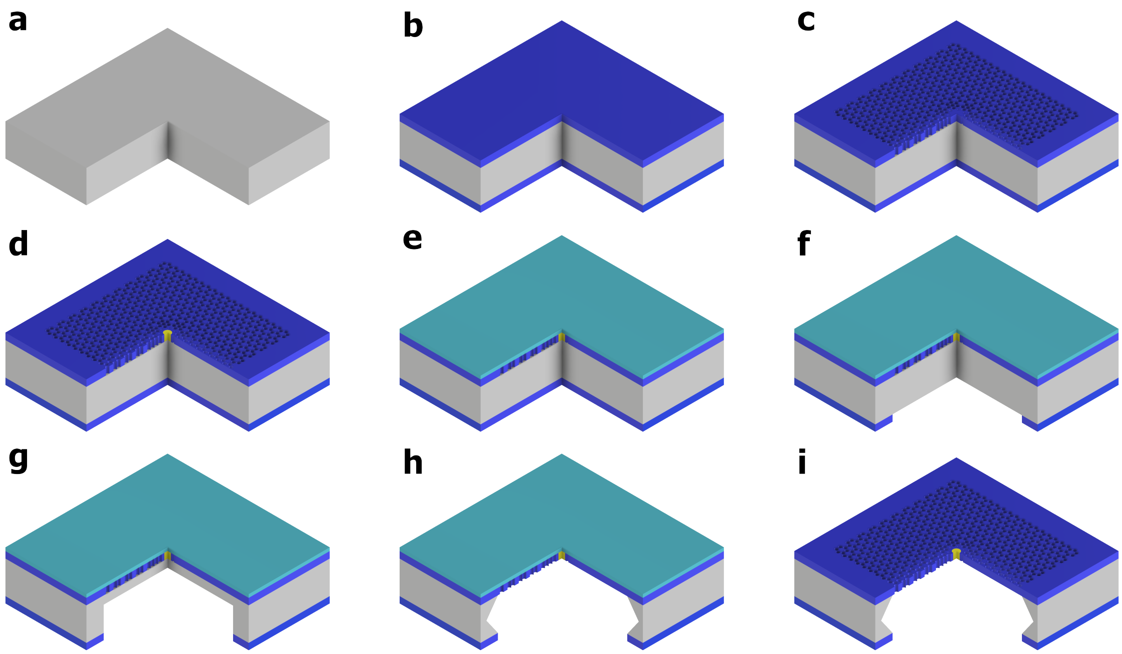

Figure 7.1: Fabrication process of a phono/photonic crystal membrane. Layer thicknesses are not to scale. Grey: silicon, 525 μm. Blue: high-stress silicon nitride, 25-100 nm (depending on the device). Yellow: photonic crystal. Light blue: low-stress silicon nitride, 100 nm.

fabricated membranes using wafers coated with 25, 50, 75 and 100 nm of silicon nitride. The nitride coating is done using low-pressure chemical vapor deposition (LPCVD), which yields a uniform film thickness, but more importantly, a high tensile stress (> 800 MPa) in the nitride. The high stress is crucial for the mechanical performance of the membranes, as discussed in section 5.3.1.

(c) Patterning the phononic crystal

We first cleave the nitride coated wafer into square chips that are 15 mm on a side. Each of these chips will have 4 membrane devices. To pattern the phononic crystal into the top silicon nitride layer, first we create a photoresist mask on the chip by using contactless photolithography. The nitride that is not protected by the photoresist is removed using an inductively coupled plasma (ICP) etch with a mixture of CF_4, CHF_3, and O_2 gases. After the etch, we remove the photoresist mask by first cleaning the chip with solvents (acetone and isopropanol) and then submerging it in a mixture of sulfuric acid and hydrogen peroxide, known as piranha solution. The piranha clean removes any photoresist residue, priming the surface for the next lithography step.

(d) Patterning the photonic crystal

To pattern the photonic crystal, we first create another resist mask on the top nitride layer. We define the resist mask at the center of the phononic crystal using electron beam lithography. The minimum feature size of our devices (see section 6.5) can actually be achieved with DUV photolithography, but by using electron beam lithography we have the capacity to modify the patterns without the need of fabricating a new photomask. This is necessary when tuning the fabrication parameters to optimize the performance of the photonic crystal. Once the resist mask is created, the pattern is etched into the silicon nitride using the same $CF_4/CHF_3/O_2$ ICP etch as before. Finally, the resist is removed with solvents and piranha solution.

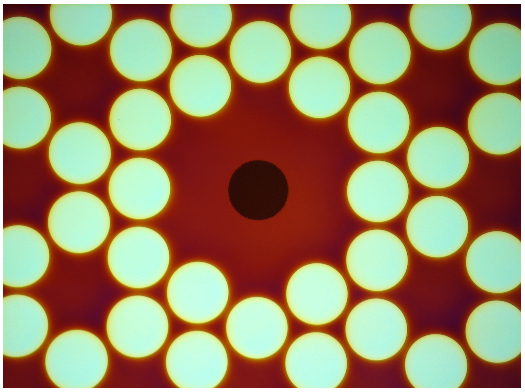

Figure 7.2: Microscope image of the front side of a photo/phononic membrane. The red region is the silicon nitride that has been patterned with the phononic and photonic crystal holes. The photonic crystal holes cannot be resolved at this magnification. The membrane is still attached to the silicon substrate, which appear

(e) Deposition of low-stress silicon nitride protective layer

Next, we deposit a layer of protective silicon nitride on the top surface of the chip. The deposition is done using plasma-enhanced chemical vapor deposition (PECVD). Compared to the initial LPCVD silicon nitride layers, the protection layer has a significantly lower stress (200 - 400 MPa) and has much faster etch rates. This layer will protect the high-stress silicon nitride during the release step of the process.

(f) Patterning of bottom silicon nitride

Up until this point in the fabrication, the top side of the chip is never put in contact with any hard surface to prevent it from getting scratched. In order to be able to pattern the bottom nitride layer, we coat the top surface of the chip with photoresist. Now the chip can be safely flipped over. Next, we use contact photolithography on the bottom face of the chip to define a photoresist mask with a square opening in it. The opening will serve to etch the silicon from underneath the membrane.

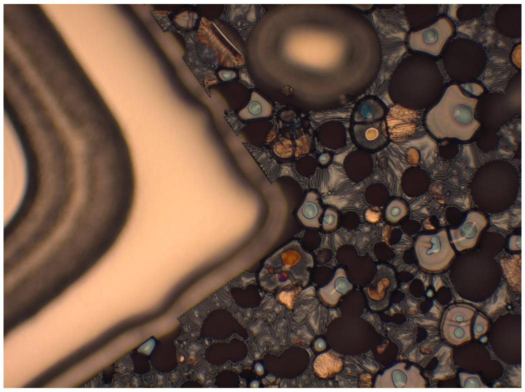

Figure 7.3: Image of the photoresist mask during the deep silicon etch. If too much moisture remains in the photoresist, small holes form in the mask as a result of bubbles that rise to the surface. This is detrimental to the fabrication process, as the silicon frame is etched through the holes. The formation of bubbles can be largely prevented by “baking” the photoresist a few seconds extra during the lithography step.

(g) Deep etch of silicon

Having opened a square hole in the back of the chip, we perform a deep reactive-ion etch (DRIE) of the silicon using the Bosch process. This etch process is very rough, so we cannot employ it to fully remove the silicon from underneath the membrane. Therefore we stop the etch when roughly 100 μm of silicon are left. Subsequently, the resist on both sides of the chip is removed with solvents and piranha solution.

(h) Membrane release

To remove the remaining silicon beneath the membrane, we perform a wet etch with potassium hydroxide (KOH) at 80° for 3.5 hours. This process is anisotropic, etching preferentially along the $\langle 111 \rangle$ planes in the silicon, which is why we obtain slanted sidewalls at the end.

High-stress silicon nitride has a slow etch rate in KOH, roughly 1 nm/hour. For our thin membranes, this is enough to drastically degrade the properties of the photonic crystal, and there are indications that prolonged exposure to KOH also roughens the surface of silicon nitride, which negatively impacts its mechanical properties (see section 5.3.1). This is why we deposit the low-stress nitride layer on the chip, which prevents the membrane from being in prolonged contact with KOH.

(i) HF cleaning

As a final step, we submerge the chip in hydrofluoric acid (HF) which quickly removes the protective nitride layer and cleans any KOH residue. We then rinse the chip with deionized water and then gently blow dry it with nitrogen gas.

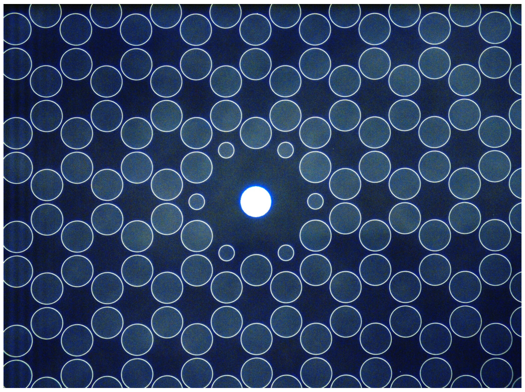

Figure 7.4: A dark field microscope images of a finished photo/phononic membrane. The glow in the central region is the result of all the edges of the photonic crystal holes being highlighted by the imaging technique.

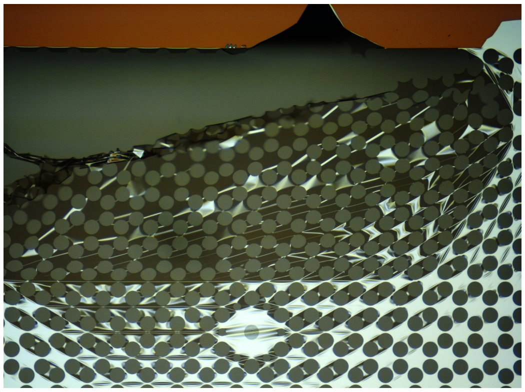

Figure 7.5: A broken photo/phononic membrane. Sometimes the devices tear during the release step of the fabrication, from turbulence in the liquid, surface tension at the liquid-air interface, or damage in the nitride from scratches or long exposure to KOH or HF.

Chapter 8

Decoherence Measurements

In chapter 1 we stated that the ultimate goal of our work is to perform measurements of quantum decoherence using optomechanics as an experimental platform. Initially, our group explored the feasibility of schemes based on the interference of a single photon with itself, where one of the interferometer's arms contains an optomechanical cavity [69–71]. More recently, we have considered an alternative experiment that builds up on the state transfer schemes we have experimentally demonstrated (see chapter 8). In this chapter we present a summary of a theoretical proposal put forth by our group for said experiment, which we refer to as phonon interferometry [23].

8.1 Phonon interferometry

The proposed experiment consists of generating a quantum superposition state of a single phonon being shared by a pair of mechanical modes, and then measuring the state over time to extract the rate at which decoherence occurs. This is a mechanical analog of a Mach-Zehnder interferometer, where the phonon is sent through two "mechanical paths" and recombined at a later time. The experiment has six different stages:

Cooling to the ground state

In order to obtain a clear result and to have the least amount of added noise from heating throughout the experiment, both mechanical modes must be cooled to their motional ground state. For our devices with mechanical frequencies in the order of 1 MHz, this amounts to reaching temperatures of a few μK. Our cryostat can only achieve temperatures down to 100 mK, so the remaining stretch needs to be done through standard optomechanical cooling (see section 2.4.1). Once both mechanical modes have been cooled, the state of our system can be described by

$$|\psi\rangle = |0\rangle_c |0\rangle_1 |0\rangle_2 \,, \tag{8.1}$$

where the subscripts c, 1 and 2 refer to the cavity and mechanical modes 1 and 2 respectively.

Creation of a single-phonon Fock state

The next step involves adding one quantum of energy to one of the mechanical modes. Since we work with harmonic oscillators this operation requires the use of a non-linear element, for example, a qubit [2], that allows us to transition from states $|0\rangle$ to $|1\rangle$ without populating higher rungs of the harmonic ladder of Fock states. We generate this single phonon using a post-selection scheme [12, 72]. First, by sending a weak blue-detuned pulse into the cavity that couples the cavity mode to mechanical mode 1, the two-mode squeezing optomechanical interaction (see section 2.4.2) generates the following (unnormalized) state

$$|\psi\rangle \approx |0\rangle_c |0\rangle_1 + \sqrt{p}\,|1\rangle_c |1\rangle_1 + p\,|2\rangle_c |2\rangle_1 + \mathcal{O}(p^{3/2}), \tag{8.2}$$

where we have ignored mechanical mode 2 for now since it remains in the ground state. Here p is the probability that the system is in the single photon-phonon pair state. By controlling the total energy contained in the pulse, we can make $p \ll 1$, so that the components of order p and higher have a negligible contribution, resulting in

$$|\psi\rangle \approx |0\rangle_c |0\rangle_1 + \sqrt{p}\, |1\rangle_c |1\rangle_1 . \tag{8.3}$$

In order to get rid of the vacuum component of our state, we can make a projective measurement on the system by monitoring the output of the cavity with a single-photon photodetector (SPD). If we place a very narrow filter before the detector that is tuned to the cavity resonance, only photons that were downconverted from interacting with the mechanical mode can pass through. Then, the detection of a single photon resonant with the cavity heralds the creation of single phonon Fock state in the mechanical mode

$$|\psi\rangle = |0\rangle_c |1\rangle_1 |0\rangle_2 . \tag{8.4}$$

Generation of a mechanical superposition state

Now that we have a single phonon in mechanical mode 1, we need to generate the superposition state whose decoherence we want to measure. We can accomplish this task by employing one of the state transfer schemes we discussed in sections 3.1 and 3.2 to implement a beamsplitter interaction between the mechanical modes. By controlling the duration of the interaction, we can achieve a partial swap of the single phonon, after which the state of the system is

$$|\psi\rangle = \frac{1}{\sqrt{2}} |0\rangle_c \left(|1\rangle_1 |0\rangle_2 - i\, |0\rangle_1 |1\rangle_2 \right) . \tag{8.5}$$

The relative phase between the two components of the state depends on the specific implementation of the swapping operation. We discuss this in more detail in section 8.1.3, but for now, we will keep the phase that results when using the two-tone swapping scheme. Now the single phonon is in a superposition of being in either mechanical mode.

Free time evolution

Having prepared the mechanical superposition state, the system is left to evolve freely. In the absence of any external interaction, each mechanical mode evolves under the standard harmonic oscillator Hamiltonian. Assuming non-degenerate mechanical modes with frequencies Ω_1 and Ω_2 as before, a relative phase is acquired between the two components of our state. After a time τ, the state of the system is

$$|\psi(\tau)\rangle = \frac{1}{\sqrt{2}} |0\rangle_c \left(|1\rangle_1 |0\rangle_2 - i e^{-i(\Omega_2 - \Omega_1)\tau} |0\rangle_1 |1\rangle_2 \right), \tag{8.6}$$

where we have left out an irrelevant common phase factor. During this time, the coherence of the state of the system will begin to deteriorate due to a finite coupling to the environment, or by novel decoherence mechanisms.

Second partial swap

Now we perform a second partial swap between the mechanical modes. If the state remained coherent, after this second partial swap we will have

$$|\psi\rangle = |0\rangle_c \left[-\sin\left(\frac{\phi}{2}\right) |1\rangle_1 |0\rangle_2 + \cos\left(\frac{\phi}{2}\right) |0\rangle_1 |1\rangle_2 \right]. \tag{8.7}$$

where $\phi = (\Omega_2 - \Omega_1)\tau$. On the other hand, if during the time τ the phonon collapsed to either mechanical mode 1 or 2, the second partial swap will again place the system in a mechanical superposition, described by one of the following states

$$|\psi\rangle = \frac{1}{\sqrt{2}} |0\rangle_c \left(|1\rangle_1 |0\rangle_2 \mp i\, |0\rangle_1 |1\rangle_2 \right), \tag{8.8}$$

where the sign depends on whether the state had collapsed to mechanical mode 1 or 2. Here we have assumed that there is a preferred basis onto which the system will collapse, in this case: $|0\rangle_c |1\rangle_1 |0\rangle_2$ or $|0\rangle_c |0\rangle_1 |1\rangle_2$. The process of einselection, which attempts to explain how a preferred basis is chosen, goes beyond the scope of this work, but a discussion can be found in [3].

Readout of the phonon population

The last stage of the experiment consists of measuring the phonon population in one of the mechanical modes. We do so with a similar approach to the initial generation of a single phonon, except this time we use a strong red-detuned pulse to couple the cavity mode to mechanical mode 1 [12, 72]. The beamsplitter interaction (see section 2.4.1) exchanges excitations between the optical and mechanical modes. If mechanical mode 1 is populated with a phonon, a photon can be upconverted to be resonant with the cavity, and after leaking out it can pass through our narrow filter and reach the SPD. Then, the detection probability of a photon will be related to the occupation of mechanical mode 1. By repeating the experiment multiple times for different waiting periods, we can recreate how the coherence of the system decays over time.

8.1.1 Expected results

Let us consider the ideal case where every red-detuned pulse we send has 100% readout efficiency. For a state that remained coherent during the waiting period between the partial swap operations, we expect to see a sinusoidally varying photon detection

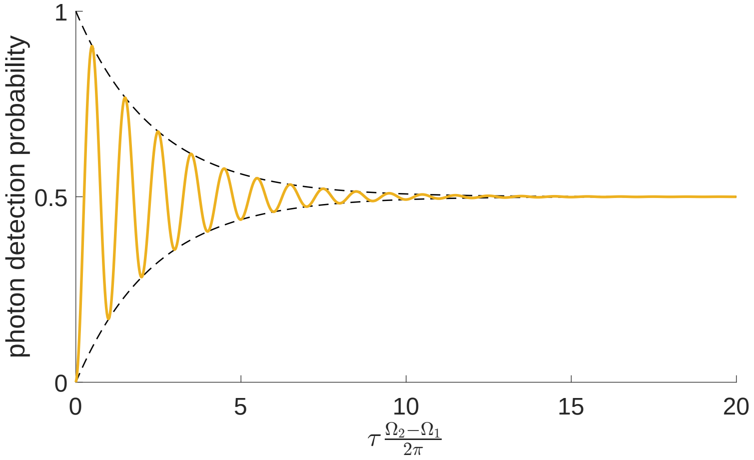

Figure 8.1: Expected photon detection probability as a function of waiting time between partial swap operations. At short times the oscillatory behaviour dominates, implying the state remained coherent. At longer times the oscillation dies out and we observe a constant detection probability.

probability. From Eqn. 8.7 we see that the readout pulse creates the state

$$|\psi\rangle_{nd} = -\sin\left(\frac{\phi}{2}\right)|1\rangle_c|0\rangle_1|0\rangle_2 + \cos\left(\frac{\phi}{2}\right)|0\rangle_c|0\rangle_1|1\rangle_2\,, \tag{8.9}$$

which we have labeled with a subscript for "no decoherence". For the case when the state did collapse, from Eqn. 8.8 we see that the readout pulse instead places the system in either of the following states

$$|\psi\rangle_d = \frac{1}{\sqrt{2}}\left(|1\rangle_c|0\rangle_1|0\rangle_2 \mp i\,|0\rangle_c|0\rangle_1|1\rangle_2\right), \tag{8.10}$$

with a subscript that stands for "decoherence", and where once again the sign depends on whether the state had collapsed to mechanical mode 1 or 2. Such a state would result in a 50% photon detection probability. Then, the general state of the system should be a combination of the two possibilities, weighted by a probability of decoherence $p_d = 1 - e^{-\gamma_d\tau}$, with γ_d being the decoherence rate. This is described by the following density matrix

$$\rho = (1 - p_d) \left|\psi\right\rangle_{nd} \left\langle\psi\right|_{nd} + p_d \left|\psi\right\rangle_{d} \left\langle\psi\right|_{d} . \tag{8.11}$$

From this, the photon detection probability is simply $\left\langle 1\right|_c \rho \left|1\right\rangle_c = (1-p_d)\sin^2(\phi/2)+p_d/2$. Since p_d transitions from 0 to 1 as τ increases, we should initially observe oscillatory behaviour that decays at longer times, as shown in Fig. 8.1. The oscillations in the photon detection probability are the crucial indication of the coherence of the system, and the decay of their amplitude will directly measure the decoherence rate of the system.

8.1.2 Experimental considerations

It is important to stress that the description we have presented is only meant to illustrate the concept of phonon interferometry, and for simplicity we have neglected all sources of dissipation. Nevertheless, with the exception of a thermalization of the phonon populations to a non-zero temperature environment, our simplified model displays the main features that would be expected. A more complete description of phonon interferometry that includes dissipation is given in [23].

In broad terms, the general condition for the proposed experiment to be feasible is that the total duration of the state manipulation and readout stages is shorter than the decoherence rate of the system. The most important parameter to satisfy this is the single-photon optomechanical coupling rate of each of the mechanical modes.

Detection

The experiment does not require a photon detection efficiency of unity to achieve a significant visibility of the coherent oscillations [23], but the detection efficiency of the entire setup should be well characterized in order to properly normalize the detection probability of a photon. Another important aspect to consider is the filter placed before the SPD. This filter must be able to block out the light of the detuned pulses that are used for state preparation and readout. We estimate that for a system with the same mechanical parameters we listed in table 3.1, a detection efficiency of 20%, and a SPD with a dark count rate of 10 photons/second, a cascade of 3 or 4 Fabry-Pérot filter cavities, each with a linewidth of 10 kHz, would provide the necessary filtering.

8.1.3 Partial transfer protocols

The partial swap operations required for the experiment can be implemented using either of the state swap schemes from sections 3.1 and 3.2. For the case of two-tone swapping, recall that the interaction is given by the Hamiltonian

$$H_{int} = J(\hat{b}_1^\dagger \hat{b}_2 + \hat{b}_1 \hat{b}_2^\dagger). \tag{8.12}$$

Under this interaction, our initial single phonon state 8.4 evolves as

$$|\psi(t)\rangle = |0\rangle_c \left[\cos\left(\frac{Jt}{\hbar}\right) |1\rangle_1 |0\rangle_2 - i \sin\left(\frac{Jt}{\hbar}\right) |0\rangle_1 |1\rangle_2 \right]. \tag{8.13}$$

To implement the partial swap, we simply need to set the pump parameters and duration such that $Jt/\hbar = \pi/4$. This will result in the desired superposition state 8.5.

An alternative way of performing the partial swap is by resorting to fractional STIRAP (f-STIRAP) [73]. In this variation of the STIRAP scheme, the mixing angle of the dark mode is “rotated” to an intermediate value between 0 and $\pi/2$ by shaping the pulses such that they decay together with a fixed ratio. As before, the dark mode is described by

$$\Phi_0(t) = [\cos\theta \, \hat{b}_1, \, 0, \, -\sin\theta \, \hat{b}_2]^T. \tag{8.14}$$

Also recall that the mixing angle is given by $\tan\theta = g_1/g_2$. To achieve the partial swap, we need to end the protocol with $\theta(t) = \pi/4$, which amounts to $g_1(t)/g_2(t) = 1$. Figure 8.2 depicts a pulse sequence that fulfills this condition, along with the expectation value of the phonon population of each mechanical mode. As with standard STIRAP, f-STIRAP has the advantage of being robust against optical losses and small variations in the driving pulses (intensities, pulse shapes, pulse widths, pulse delay).

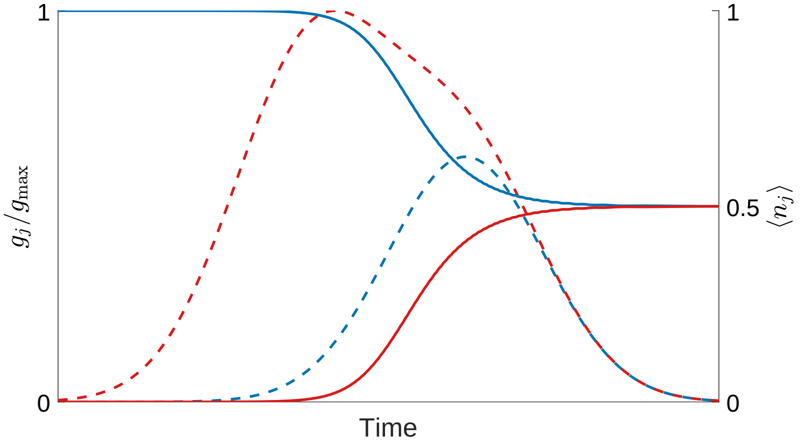

Figure 8.2: Pulse sequence to perform f-STIRAP. The phonon expectation value of mode 1 (2) is shown as a solid blue (red) line. The corresponding coupling rates are shown as dashed lines.

Chapter 9

Conclusion and Outlook

In this work, we have presented an optomechanical system as a suitable platform for the study of quantum decoherence. We discussed how the optomechanical interaction enables the control and measurement of the motional state of mechanical resonators, and how this can be exploited to measure the decoherence rate of a quantum superposition state in an interferometry experiment.

We have shown that significant technological progress has been achieved with membrane-in-the-middle optomechanical systems through the use of periodic structures. We have employed phononic crystals to drastically improve the mechanical quality factor of our silicon nitride resonators by mitigating bending losses and reducing the coupling to the substrate from which they are suspended. At the same time, we have enhanced the optomechanical coupling rate of our devices by patterning them with photonic crystals to improve their reflectivity. With such improvements, the parameters of our system should now be sufficient to make our proposed experiment feasible.

Looking forward, we have already began efforts in collaboration with professor Ania Jayich's group to fabricate phononic crystal membranes out of diamond. Compared to silicon nitride, diamond is a much harder material to use for manufacturing mechanical resonators. However, the advantages of diamond make the effort worthwhile. Being a crystalline solid, membranes fabricated out of diamond could potentially have higher intrinsic mechanical quality factors. More importantly, diamond's low optical absorption and good thermal conductivity would further enhance the robustness of our experiment at cryogenic temperatures. As of the writing of this work, the first fabrication runs are already underway.

Appendix A

Numerical Simulation Methods

In the present work we have presented many results obtained from numerical calculations. For sections 5.4 and 6 in particular, we have relied heavily on numerical methods for the computation of band structures, mode shapes and profiles, reflection spectra and design parameters. This appendix will give a short description of the different numerical tools that we employed.

All numerical methods involve some kind of discretization of the simulated domain. After the discretization is carried out, the original problem, usually stated in the form of partial differential equations, can be recast into a set of coupled algebraic equations which can be solved using linear algebra techniques. The numerical methods that we employ differ by the type of discretization that is performed and by the domain on which they solve the problem (time or frequency). Each of these has its own advantages and disadvantages and is better suited for a particular type of problem.

A.1 Finite Element Method (FEM)

The Finite Element Method is a general numerical method widely employed for the solution of many problems in engineering, particularly in the fields of structural mechanics, fluid mechanics, heat flow and electrodynamics [74]. The method receives its name from the fact that it relies on the discretization of space into a finite number of irregular elements, usually triangles in 2D and tetrahedra in 3D (see Fig. A.1). The solution to the problem, for example, a scalar field of the temperature throughout a body, or a vector field of the velocity of a fluid, is approximated by a collection of basis functions, usually low-order polynomials, defined within each element [75]. Fig. A.2 shows a 1D representation of this procedure, where an unknown function $f(x)$ is approximated by $\tilde{f}$, a sum of linear basis functions ψ_n weighted by the coefficients f_n

$$\tilde{f} = \sum_{n=0}^{N} f_n \psi_n. \tag{A.1}$$

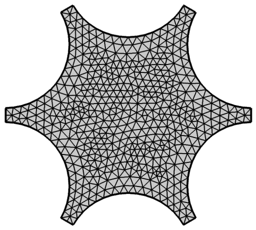

Figure A.1: The 2D mesh for a unit cell of a phononic crystal membrane. The mesh is formed by irregular triangular elements.

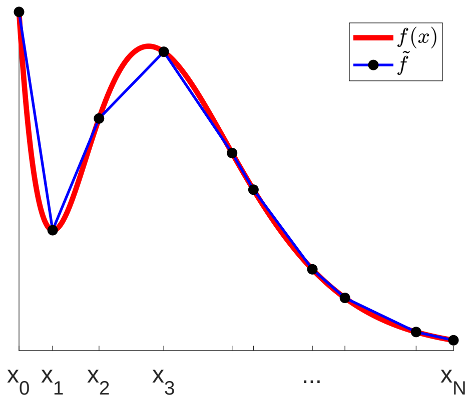

Figure A.2: An unknown function $f(x)$ is approximated by stitching up a discrete set of linear basis functions.

In this work, we employ FEM for the computation of the band structure and mechanical mode shapes of a phononic crystal membrane. As discussed in section 5.4, the quantity of interest is the displacement field $\mathbf{u}(x, y, z, t)$, whose dynamics are governed by the following equation of motion

$$\frac{E}{2(1+\nu)}\left(\nabla^2\mathbf{u} + \frac{1}{1-2\nu}\nabla(\nabla\cdot\mathbf{u})\right) = \rho\frac{\partial^2\mathbf{u}}{\partial t^2}. \tag{A.2}$$

The LHS of this equation can be regarded as involving a differential operator $\hat{\Theta}$ that computes only spatial derivatives of $\mathbf{u}$. In a discretized framework where we approximate $\mathbf{u}$ by $\tilde{\mathbf{u}}$ as in equation A.1, $\hat{\Theta}$ is a sparse matrix that connects each coefficient $\mathbf{u}_n$ solely to other coefficients $\mathbf{u}_m$ that are spatially adjacent to it. Furthermore, by assuming harmonic solutions $\mathbf{u}(x, y, z, t) = \mathbf{u}(x, y, z)e^{i\omega t}$, we can tackle the problem in the frequency domain as an eigenvalue problem:

$$\hat{\Theta}\tilde{\mathbf{u}} = -\omega^2\rho\tilde{\mathbf{u}}, \tag{A.3}$$

for the differential operator $\hat{\Theta}$, whose eigenvectors and eigenvalues correspond to the structure's mode shapes and frequencies, respectively. If we impose periodic boundary conditions, we can obtain the Bloch modes of a periodic system from the simulation of a unit cell of the lattice (see section 4.2). Finally, by sweeping the k-vector of the Bloch modes along the edge of the IBZ, we can compute the band structure of the system.

The irregular mesh used in FEM grants the flexibility of decreasing the size of the mesh only around boundaries and small features, allowing us to accurately model those regions without greatly increasing the computational cost of the simulation. This is particularly useful when dealing with geometries that are irregular or have features of different scales.

The advantages of FEM come at the cost of a more complicated implementation, as compared to other methods. Additionally, the implementation usually requires a problem-dependent optimization for aspects such as the order of the basis functions or the meshing algorithm.

We used the software *COMSOL Multiphysics*®[76] to carry out all the FEM computations in this work. Many other CAD and computation software packages (open and closed source) have FEM implementations.

A.2 Finite-difference Time-domain Method (FDTD)

The finite-difference time-domain method is a widely used technique in computational electrodynamics. As the name implies, the method computes the evolution of electric and magnetic fields **E** and **H** in time, according to Maxwell's equations

$$\frac{\partial \mathbf{D}}{\partial t} = \nabla \times \mathbf{H}, \tag{A.4}$$

$$\frac{\partial \mathbf{H}}{\partial t} = -\frac{1}{\mu_0}\nabla \times \mathbf{E}, \tag{A.5}$$

where $\mathbf{D}(\omega) = \epsilon(\omega)\mathbf{E}(\omega)$ [77]. The method relies on the discretization of space and time into a possibly non-uniform rectangular mesh. The spatial derivatives of the fields are approximated as their difference across a cell, which are then used to propagate the fields forward in time. Normally, the fields are solved for in a staggered manner, meaning that at a given time step, the spatial derivatives of **E** are used to propagate **H** in time, and in the subsequent time step the reverse takes place, and so on in an cyclic manner [78].

An important advantage of FDTD is that one can obtain broadband results from a single simulation. Since it is a time-domain method, one can use a short pulse to excite the system and then perform a Fourier transform of the computed fields. The method is also convenient for visualizing the fields as they evolve in time, which is often useful for gaining an intuition about a process or phenomenon.

A limitation of the FDTD method comes from the fact that it is computed over a rectangular grid. If a fine mesh resolution is desired in a certain region, the mesh resolution must be increased throughout the entire simulated domain. This can result in dense meshes in regions where it is not necessary. Furthermore, FDTD only supports rectangular domains, which presents complications when working with non-rectangular geometries and boundary conditions.

In this work, we employed FDTD to compute band structures, mode profiles and reflectance spectra for a photonic crystal slab. In all of these calculations, a single unit cell of the structure is simulated surrounded by periodic boundaries on its sides and absorbing boundaries above and below (see Fig. A.3). The periodic boundaries allow us to simulate a PCS that extends infinitely along the plane of the slab.

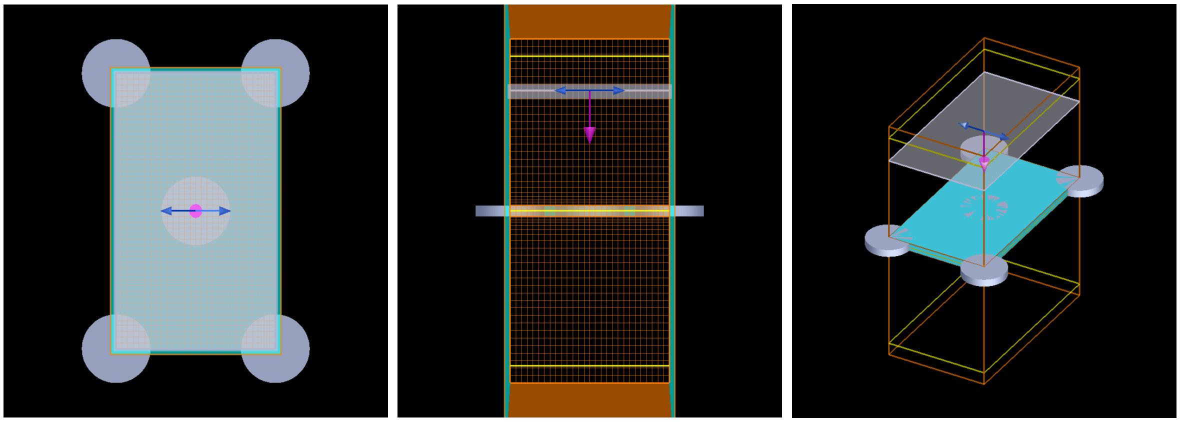

Figure A.3: Multiple perspectives of the FDTD cell used to simulate an infinite PCS. A boundary is shown as orange (blue) if it is periodic (absorbing). The grey layer in the center and right panels shows where a plane wave is launched, and the blue and pink arrows indicate its polarization and direction of propagation, respectively.

To calculate band structures and mode profiles, we excite the structure with randomly placed and oriented dipole sources. The fields are monitored in time, and by taking the Fourier transform of the signal we can extract its power spectrum and find the resonance frequency and linewidth of the modes of the structure. In a similar way, we obtain cross-sections of the mode profiles by placing a uniform distribution of monitors along a plane of the simulated domain and then performing a Fourier transform. On the other hand, to obtain reflectance and transmittance spectra, we launch a plane wave towards the PCS and monitoring the total power that flows across the two boundaries that are parallel to the slab.

We also simulate a finite sized PCS excited by a Gaussian source. These simulations cannot be performed on a single lattice cell, instead, the entire extent of the PCS must be included in the simulation domain. For this task it is advisable to use cluster computing resources, since the simulations can get very computationally expensive. While the simulation of a single lattice cell usually completes within half a minute, the simulation of a full device of realistic dimensions can take up to a week.

We used the software *Lumerical*®[79] for all our FDTD computations. A widely used open source alternative is *MEEP*©[80].

A.3 Rigorous Coupled-Wave Analysis (RCWA)

The method of rigorous coupled-wave analysis is another commonly used technique in computational electrodynamics, particularly for the study of diffraction phenomena [81]. RCWA is a frequency-domain method that discretizes the simulated system into layers, each of which is assumed to be uniform along the direction of wave propagation [82]. The eigenmodes of each layer are expanded in a Fourier basis (as a sum of plane waves) and propagated up to the next boundary. The method is semi-analytic, in that the only approximation is made with the necessary truncation of the number of basis functions used. After calculating all the eigenmode expansions, the first layer is excited with a plane wave, and at each layer boundary the scattering matrix formalism [83] is employed to make the fields match, thus yielding a self-consistent global solution.

By construction, the method is suitable for calculations involving layered media, possibly comprised of many layers, such as 1D photonic crystals. Furthermore, the use of a Fourier decomposition, makes it straightforward to treat layers that are periodic in the transverse direction using Bloch formalism, as discussed in section 4.2. This makes RCWA useful for studying diffraction gratings and photonic crystals. The method can also be used with no input source to calculate the modes and dispersion relation of the entire structure.

Our usage of RCWA is restricted to systems with only three layers, namely a PCS sandwiched by two semi-infinite air regions. We have employed RCWA mainly for finding the optimal design parameters of the PCS. Given a slab thickness and operating wavelength, we perform a parameter sweep of the lattice constant and hole radius to obtain the combination that maximizes the reflectivity.

For this work we employed the open source solver S^4©[82].

A.4 Convergence

For any type of numerical simulation, it is good practice to perform a convergence study. This consists of first creating a coarse simulation that models the essential physics of the problem, and then varying the simulation's parameters (such as mesh resolution, thickness of absorbing boundaries, etc.) until there is no further change in the result, to within a desired tolerance. For all the numerical simulations that were carried out in this work, we performed convergence studies for all the relevant parameters, including the extension of the simulated domain, the size of the mesh cells/elements, and the number of decomposition functions.

Bibliography

[1] J. R. Friedman, V. Patel, W. Chen, S. K. Tolpygo, and J. E. Lukens, “Quantum superposition of distinct macroscopic states”, Nature **406**, 43–46 (2000).

[2] A. D. O’Connell, M. Hofheinz, M. Ansmann, R. C. Bialczak, M. Lenander, E. Lucero, M. Neeley, D. Sank, H. Wang, M. Weides, J. Wenner, J. M. Martinis, and A. N. Cleland, “Quantum ground state and single-phonon control of a mechanical resonator”, Nature **464**, 697–703 (2010).

[3] W. H. Zurek, “Decoherence and the transition from quantum to classical”, Physics Today **44**, 36–44 (1991).

[4] M. A. Schlosshauer, *Decoherence and the quantum-to-classical transition* (2007).

[5] R. Penrose, “On gravity’s role in quantum state reduction”, General relativity and gravitation **28**, 581–600 (1996).

[6] G. C. Ghirardi, P. Pearle, and A. Rimini, “Markov processes in hilbert space and continuous spontaneous localization of systems of identical particles”, Physical Review A **42**, 78–89 (1990).

[7] M. Aspelmeyer, T. J. Kippenberg, and F. Marquardt, “Cavity optomechanics”, Reviews of Modern Physics **86**, 1391–1452 (2014).

[8] A. Jöckel, A. Faber, T. Kampschulte, M. Korppi, M. T. Rakher, and P. Treutlein, "Sympathetic cooling of a membrane oscillator in a hybrid mechanical–atomic system", Nature Nanotechnology **10**, 55–59 (2015).

[9] T. Bodiya, V. Sudhir, C. Wipf, N. Smith, A. Buikema, A. Kontos, H. Yu, and N. Mavalvala, "Sub-hertz optomechanically induced transparency with a kilogram-scale mechanical oscillator", Physical Review A **100**, 013853 (2019).

[10] M. Evans, S. Gras, P. Fritschel, J. Miller, L. Barsotti, D. Martynov, A. Brooks, D. Coyne, R. Abbott, R. X. Adhikari, K. Arai, R. Bork, B. Kells, J. Rollins, N. Smith-Lefebvre, G. Vajente, H. Yamamoto, C. Adams, S. Aston, J. Betzweiser, V. Frolov, A. Mullavey, A. Pele, J. Romie, M. Thomas, K. Thorne, S. Dwyer, K. Izumi, K. Kawabe, D. Sigg, R. Derosa, A. Effler, K. Kokeyama, S. Ballmer, T. J. Massinger, A. Staley, M. Heinze, C. Mueller, H. Grote, R. Ward, E. King, D. Blair, L. Ju, and C. Zhao, "Observation of parametric instability in advanced LIGO", Physical Review Letters **114**, 161102 (2015).

[11] J. V. Cady, O. Michel, K. W. Lee, R. N. Patel, C. J. Sarabalis, A. H. Safavi-Naeini, and A. C. Bleszynski Jayich, "Diamond optomechanical crystals with embedded nitrogen-vacancy centers", Quantum Science and Technology **4**, 024009 (2019).

[12] S. Hong, R. Riedinger, I. Marinković, A. Wallucks, S. G. Hofer, R. A. Norte, M. Aspelmeyer, and S. Gröblacher, "Hanbury brown and twiss interferometry of single phonons from an optomechanical resonator", Science **358**, 203–206 (2017).

[13] O. Romero-Isart, A. C. Pflanzer, F. Blaser, R. Kaltenbaek, N. Kiesel, M. Aspelmeyer, and J. I. Cirac, "Large quantum superpositions and interference of massive nanometer-sized objects", Physical Review Letters **107**, 020405 (2011).

[14] D. F. Walls and G. J. Milburn, *Quantum optics*, 2nd ed (Springer, Berlin, 2008), 425 pp.

[15] S. Weis, R. Rivière, S. Deléglise, E. Gavartin, O. Arcizet, A. Schliesser, and T. J. Kippenberg, “Optomechanically induced transparency”, Science **330**, 1520–1523 (2010).

[16] F. M. Buters, F. Luna, M. J. Weaver, H. J. Eerkens, K. Heeck, S. de Man, and D. Bouwmeester, “Straightforward method to measure optomechanically induced transparency”, Optics Express **25**, 12935 (2017).

[17] A. M. Jayich, J. C. Sankey, B. M. Zwickl, C. Yang, J. D. Thompson, S. M. Girvin, A. A. Clerk, F. Marquardt, and J. G. E. Harris, “Dispersive optomechanics: a membrane inside a cavity”, New Journal of Physics **10**, 095008 (2008).

[18] D. C. Newsom, F. Luna, V. Fedoseev, W. Löffler, and D. Bouwmeester, “Optimal optomechanical coupling strength in multimembrane systems”, Physical Review A **101**, 033829 (2020).

[19] R. W. Andrews, R. W. Peterson, T. P. Purdy, K. Cicak, R. W. Simmonds, C. A. Regal, and K. W. Lehnert, “Bidirectional and efficient conversion between microwave and optical light”, Nature Physics **10**, 321–326 (2014).

[20] H. Xu, D. Mason, L. Jiang, and J. G. E. Harris, “Topological energy transfer in an optomechanical system with exceptional points”, Nature **537**, 80–83 (2016).

[21] H. Xu, L. Jiang, A. A. Clerk, and J. G. E. Harris, “Nonreciprocal control and cooling of phonon modes in an optomechanical system”, Nature **568**, 65–69 (2019).

[22] N. V. Vitanov, A. A. Rangelov, B. W. Shore, and K. Bergmann, “Stimulated raman adiabatic passage in physics, chemistry, and beyond”, Reviews of Modern Physics **89**, 015006 (2017).

[23] M. J. Weaver, D. Newsom, F. Luna, W. Löffler, and D. Bouwmeester, “Phonon interferometry for measuring quantum decoherence”, Physical Review A **97**, 063832 (2018).

[24] M. J. Weaver, F. Buters, F. Luna, H. Eerkens, K. Heeck, S. Man, and D. Bouwmeester, “Coherent optomechanical state transfer between disparate mechanical resonators”, Nature Communications **8**, 824 (2017).

[25] V. Fedoseev, F. Luna, W. Löffler, and D. Bouwmeester, “Stimulated raman adiabatic passage in optomechanics”, arXiv:1911.11464 [physics, physics:quant-ph] (2019).

[26] L. F. Buchmann and D. M. Stamper-Kurn, “Nondegenerate multimode optomechanics”, Physical Review A **92** (2015).

[27] L. Tian, “Adiabatic state conversion and pulse transmission in optomechanical systems”, Physical Review Letters **108**, 153604 (2012).

[28] C. Dong, V. Fiore, M. C. Kuzyk, and H. Wang, “Optomechanical dark mode”, Science **338**, 1609–1613 (2012).

[29] Y.-D. Wang and A. A. Clerk, “Using interference for high fidelity quantum state transfer in optomechanics”, Physical Review Letters **108**, 153603 (2012).

[30] M. Bhattacharya and P. Meystre, “Multiple membrane cavity optomechanics”, Physical Review A **78** (2008).

[31] A. Xuereb, C. Genes, and A. Dantan, “Collectively enhanced optomechanical coupling in periodic arrays of scatterers”, Physical Review A **88**, 053803 (2013).

[32] C. Kittel, *Introduction to solid state physics*, 8th ed (Wiley, Hoboken, NJ, 2005), 680 pp.

[33] H. Ibach and H. Lüth, *Solid-state physics: an introduction to principles of materials science*, 4., Advanced texts in physics (Springer, Dordrecht, 2009), 533 pp.

[34] W. Setyawan and S. Curtarolo, “High-throughput electronic band structure calculations: challenges and tools”, Computational Materials Science **49**, 299–312 (2010).

[35] B. Salski, “The unfolding of bandgap diagrams of hexagonal photonic crystals computed with FDTD”, Progress In Electromagnetics Research **27**, 27–39 (2012).

[36]L.D. Landau & E.M. Lifshitz, *Theory of elasticity* (Pergamon Press, 1970).

[37]K. D. Hjelmstad, *Fundamentals of structural mechanics* (Springer Science + Business Media, Inc., Boston, MA, 2005).

[38]S. Timoshenko, *Vibration problems in engineering*, in collab. with Osmania University and Digital Library Of India (D.Van Nostrand Company INC., 1937), 497 pp.

[39]S. S. Rao, *Mechanical vibrations*, 4th (Pearson/Prentice Hall, Upper Saddle River, N.J., 2004), xxvi+1078.

[40]S. Schmid, K. D. Jensen, K. H. Nielsen, and A. Boisen, "Damping mechanisms in high-q micro and nanomechanical string resonators", Physical Review B **84**, 165307 (2011).

[41]Q. P. Unterreithmeier, T. Faust, and J. P. Kotthaus, "Damping of nanomechanical resonators", Physical Review Letters **105**, 027205 (2010).

[42]A. H. Ghadimi, D. J. Wilson, and T. J. Kippenberg, "Dissipation engineering of high-stress silicon nitride nanobeams", arXiv:1603.01605 [cond-mat, physics:physics, physics:quant-ph] (2016).

[43]T. P. M. Alegre, A. Safavi-Naeini, M. Winger, and O. Painter, "Quasi-two-dimensional optomechanical crystals with a complete phononic bandgap", Optics express **19**, 5658–5669 (2011).

[44]Y. Tsaturyan, A. Barg, E. S. Polzik, and A. Schliesser, "Ultracoherent nanomechanical resonators via soft clamping and dissipation dilution", Nature Nanotechnology **12**, 776–783 (2017).

[45]A. H. Ghadimi, S. A. Fedorov, N. J. Engelsen, M. J. Bereyhi, R. Schilling, D. J. Wilson, and T. J. Kippenberg, "Elastic strain engineering for ultralow mechanical dissipation", Science **360**, 764–768 (2018).

[46] P.-L. Yu, T. P. Purdy, and C. A. Regal, "Control of material damping in high-q membrane microresonators", Physical Review Letters **108**, 083603 (2012).

[47] D. R. Southworth, R. A. Barton, S. S. Verbridge, B. Ilic, A. D. Fefferman, H. G. Craighead, and J. M. Parpia, "Stress and silicon nitride: a crack in the universal dissipation of glasses", Physical Review Letters **102**, 225503 (2009).

[48] S. Chakram, Y. S. Patil, L. Chang, and M. Vengalattore, "Dissipation in ultrahigh quality factor SiN membrane resonators", Physical Review Letters **112** (2014).

[49] M. J. Weaver, B. Pepper, F. Luna, F. M. Buters, H. J. Eerkens, G. Welker, B. Perock, K. Heeck, S. de Man, and D. Bouwmeester, "Nested trampoline resonators for optomechanics", Applied Physics Letters **108**, 033501 (2016).

[50] S. K. De and N. R. Aluru, "Theory of thermoelastic damping in electrostatically actuated microstructures", Physical Review B **74**, 144305 (2006).

[51] K. Kunal and N. R. Aluru, "Akhiezer damping in nanostructures", Physical Review B **84**, 245450 (2011).

[52] J. Rodriguez, S. A. Chandorkar, C. A. Watson, G. M. Glaze, C. H. Ahn, E. J. Ng, Y. Yang, and T. W. Kenny, "Direct detection of akhiezer damping in a silicon MEMS resonator", Scientific Reports **9**, 2244 (2019).

[53] G. S. MacCabe, H. Ren, J. Luo, J. D. Cohen, H. Zhou, A. Sipahigil, M. Mirhosseini, and O. Painter, "Phononic bandgap nano-acoustic cavity with ultralong phonon lifetime", arXiv:1901.04129 [cond-mat, physics:quant-ph] (2019).

[54] I. Galinskiy, Y. Tsaturyan, Y. Tsaturyan, M. Parniak, and E. S. Polzik, "Phonon counting thermometry of an ultracoherent membrane resonator near its motional ground state", Optica **7**, 718–725 (2020).

[55] P. S. J. Russell, P. Hölzer, W. Chang, A. Abdolvand, and J. C. Travers, “Hollow-core photonic crystal fibres for gas-based nonlinear optics”, Nature Photonics **8**, 278–286 (2014).

[56] M. Arcari, I. Söllner, A. Javadi, S. Lindskov Hansen, S. Mahmoodian, J. Liu, H. Thyrrestrup, E. H. Lee, J. D. Song, S. Stobbe, and P. Lodahl, “Near-unity coupling efficiency of a quantum emitter to a photonic crystal waveguide”, Physical Review Letters **113**, 093603 (2014).

[57] M. Bayindir, B. Temelkuran, and E. Ozbay, “Photonic-crystal-based beam splitters”, Applied Physics Letters **77**, 3902–3904 (2000).

[58] Z. Wang and S. Fan, “Optical circulators in two-dimensional magneto-optical photonic crystals”, Optics Letters **30**, 1989–1991 (2005).

[59] M. J. Burek, J. D. Cohen, S. M. Meenehan, N. El-Sawah, C. Chia, T. Ruelle, S. Meesala, J. Rochman, H. A. Atikian, M. Markham, D. J. Twitchen, M. D. Lukin, O. Painter, and M. Lončar, “Diamond optomechanical crystals”, Optica **3**, 1404 (2016).

[60] J. D. Joannopoulos, ed., *Photonic crystals: molding the flow of light*, 2nd ed (Princeton University Press, Princeton, 2008), 286 pp.

[61] S. Fan and J. D. Joannopoulos, “Analysis of guided resonances in photonic crystal slabs”, Physical Review B **65**, 235112 (2002).

[62] X. Chen, C. Chardin, K. Makles, C. Caër, S. Chua, R. Braive, I. Robert-Philip, T. Briant, P.-F. Cohadon, A. Heidmann, T. Jacqmin, and S. Deléglise, “High-finesse fabry–perot cavities with bidimensional si 3 n 4 photonic-crystal slabs”, Light: Science & Applications **6**, e16190–e16190 (2017).

[63] J. P. Moura, R. A. Norte, J. Guo, C. Schäfermeier, and S. Gröblacher, “Centimeter-scale suspended photonic crystal mirrors”, Optics Express **26**, 1895 (2018).

[64]B. E. A. Saleh and M. C. Teich, *Fundamentals of photonics*, 2nd ed, Wiley series in pure and applied optics (Wiley Interscience, Hoboken, N.J, 2007), 1175 pp.

[65]S. Fan, W. Suh, and J. D. Joannopoulos, "Temporal coupled-mode theory for the fano resonance in optical resonators", JOSA A **20**, 569–572 (2003).

[66]K. B. Crozier, V. Lousse, O. Kilic, S. Kim, S. Fan, and O. Solgaard, "Air-bridged photonic crystal slabs at visible and near-infrared wavelengths", Physical Review B **73**, 115126 (2006).

[67]J. Pinto Moura, "Making light jump: photonic crystals on trampoline membranes for optomechanics experiments", PhD thesis (TU Delft, 2019).

[68]S. Boutami, B. Ben Bakir, X. Letartre, J. L. Leclercq, and P. Viktorovitch, "Photonic crystal slab mirrors for an ultimate vertical and lateral confinement of light in vertical fabry perot cavities", in Photonic crystal materials and devices VIII, edited by R. M. De La Rue, C. López, M. Midrio, and P. Viktorovitch (Apr. 25, 2008), p. 69890V.

[69]W. Marshall, C. Simon, R. Penrose, and D. Bouwmeester, "Towards quantum superpositions of a mirror", Physical Review Letters **91** (2003).

[70]D. Kleckner, I. Pikovski, E. Jeffrey, L. Ament, E. Eliel, J. van den Brink, and D. Bouwmeester, "Creating and verifying a quantum superposition in a micro-optomechanical system", New Journal of Physics **10**, 095020 (2008).

[71]B. Pepper, R. Ghobadi, E. Jeffrey, C. Simon, and D. Bouwmeester, "Optomechanical superpositions via nested interferometry", Physical Review Letters **109** (2012).

[72]R. Riedinger, A. Wallucks, I. Marinković, C. Löschnauer, M. Aspelmeyer, S. Hong, and S. Gröblacher, "Remote quantum entanglement between two micromechanical oscillators", Nature **556**, 473–477 (2018).

[73] N. V. Vitanov, K.-A. Suominen, and B. W. Shore, "Creation of coherent atomic superpositions by fractional stimulated raman adiabatic passage", Journal of Physics B: Atomic, Molecular and Optical Physics **32**, 4535–4546 (1999).

[74] *Finite element method*, in *Wikipedia* (May 14, 2020).

[75] *Detailed explanation of the finite element method (FEM)*, (Feb. 21, 2017) `https://www.comsol.com/multiphysics/finite-element-method` (visited on 06/04/2020).

[76] *COMSOL: multiphysics software for optimizing designs*, COMSOL Multiphysics®, `https://www.comsol.com/` (visited on 07/09/2020).

[77] *Finite difference time domain (FDTD) solver introduction*, Lumerical Support, `http://support.lumerical.com/hc/en-us/articles/360034914633` (visited on 06/01/2020).

[78] A. Taflove, *Computational electrodynamics: the finite-difference time-domain method.* In collab. with S. C. Hagness, 3rd, Artech House antennas and propagation library (Artech House, Norwood, 2005), xxii+1006.

[79] *High-performance photonic simulation software*, Lumerical, `https://www.lumerical.com/` (visited on 07/09/2020).

[80] A. F. Oskooi, D. Roundy, M. Ibanescu, P. Bermel, J. Joannopoulos, and S. G. Johnson, "Meep: a flexible free-software package for electromagnetic simulations by the FDTD method", Computer Physics Communications **181**, 687–702 (2010).

[81] R. Bräuer and O. Bryngdahl, "Electromagnetic diffraction analysis of two-dimensional gratings", Optics Communications **100**, 1–5 (1993).

[82] V. Liu and S. Fan, "S4 : a free electromagnetic solver for layered periodic structures", Computer Physics Communications **183**, 2233–2244 (2012).

[83] D. M. Whittaker and I. S. Culshaw, "Scattering-matrix treatment of patterned multilayer photonic structures", Physical Review B **60**, 2610–2618 (1999).